Tectonics

RESEARCH ARTICLE
10.1029/2018TC005168

Key Points:
- Magnetic fabrics of carbonate rocks are sensitive strain indicators, suitable for strain field determination along major faults
- Diamagnetic fabrics of carbonate rocks indicate maximum horizontal shortening parallel to the southern segment of the Dead Sea Fault (DSF)
- The strain field close to the DSF is local, with a component of divergence

Supporting Information:
- Table S1

Correspondence to:
R. Issachar,
ranissachar@gmail.com

Citation:
Issachar, R., Levi, T., Marco, S., & Weinberger, R. (2019). Strain field associated with a component of divergent motion along the southern Dead Sea fault: Insights from magnetic fabrics. *Tectonics*, *38*. https://doi.org/10.1029/2018TC005168

Received 31 MAY 2018
Accepted 19 DEC 2018
Accepted article online 26 DEC 2018

Strain Field Associated With a Component of Divergent Motion Along the Southern Dead Sea Fault: Insights From Magnetic Fabrics

R. Issachar[1,2], T. Levi[2], S. Marco[1], and R. Weinberger[2,3]

[1]Department of Geophysics, Tel Aviv University, Tel Aviv, Israel, [2]Geological Survey of Israel, Jerusalem, Israel, [3]Department of Geological and Environmental Sciences, Ben-Gurion University of the Negev, Beer-Sheva, Israel

Abstract In order to reconstruct the strain field along the southern segment of the Dead Sea Fault (DSF) plate boundary, we analyzed the magnetic fabrics of carbonate rocks, outcropping along it. The magnetic fabrics provide a microstructural indicator that help to approximate the principal strain directions in the rocks. Our analysis includes ~900 cores from 58 sampling localities, along ~400 km of the southern DSF. We measured the magnetic fabrics of (1) pure calcite-bearing limestones that consist diamagnetic fabrics and (2) chalks with composite fabrics, which we further separated into diamagnetic and paramagnetic subfabrics, using measurements of Anisotropy of Magnetic Susceptibility at low temperatures. The results show that 87% of the diamagnetic fabrics and subfabrics are of tectonic origin. The orientations of the maximum Anisotropy of Magnetic Susceptibility axes (K_3 axes) approximately align with the maximum horizontal shortening directions along the southern segment of the DSF, differ from the remote stress direction, and are largely parallel to the main trace of the DSF. This parallelism is not related to local variations in the geometry of the faults. We suggest that the deflection of the maximum horizontal shortening parallel to the transform plate boundary is a kinematic consequence of the Sinai-Arabia relative plate motion, which expresses a component of divergence along the southern segment of the DSF. We conclude that magnetic fabrics of carbonate rocks are sensitive and reliable microstructural indicators for determination of the strain field along major fault systems.

1. Introduction

1.1. Strain Field Along Strike-Slip Plate Boundaries

Determining the strain field associated with major fault systems is challenging due to the scarcity of visible strain markers and their absence in massive rock units. We use the magnetic fabrics of rocks, which provide a micro structural strain indicators that are independent and complementary to mesostructural and macrostructural indicators (Borradaile, 1988). In this study, we reconstruct the strain field along the southern segment of the Dead Sea Fault (DSF) system (Figure 1) by measuring the magnetic fabrics of pre-DSF Eocene carbonate rocks, in which outcrop-scale strain markers are very rare.

The strain field next to strike-slip dominated plate boundaries, like the DSF and the San Andreas Fault, often deviates from the remote strain field. The deviation is often evident by formation of contractional or extensional structures perpendicular to the faults (Fossen, 2010; Fossen et al., 1994). Evidence of those kinds of structures is found along the DSF mainly in the form of extensional structures in the southern segment of the DSF system (Ben-Avraham, 1992; Garfunkel et al., 1981) and contractional structures along the northern segment of the system (Gomez et al., 2006; Weinberger, 2014). Perpendicular structures are also found near the San Andreas Fault (e.g., Mount & Suppe, 1987) and other continental strike-slip faults (e.g., Dewey et al., 1998). Zoback et al. (1987) introduce a model relating the fault strength and the relative orientation of the remote stress field. They show that for "weak" faults, the maximum horizontal compressive stress aligns parallel or perpendicular to the fault plane, resulting in transtension or transpression regimes. Tikoff and Teyssier (1994) argue that the deformation along plate boundaries must ultimately be related to the relative motion of the tectonic plates and suggest that kinematic models can adequately explain most strike-slip parallel and perpendicular structures, regardless of the fault strength. The strain field close to the DSF is not well determined. In order to examine these approaches we aim to reconstruct the strain field along the southern segment of the DSF and compare it with the regional (remote) strain field.

10.1029/2018TC005168

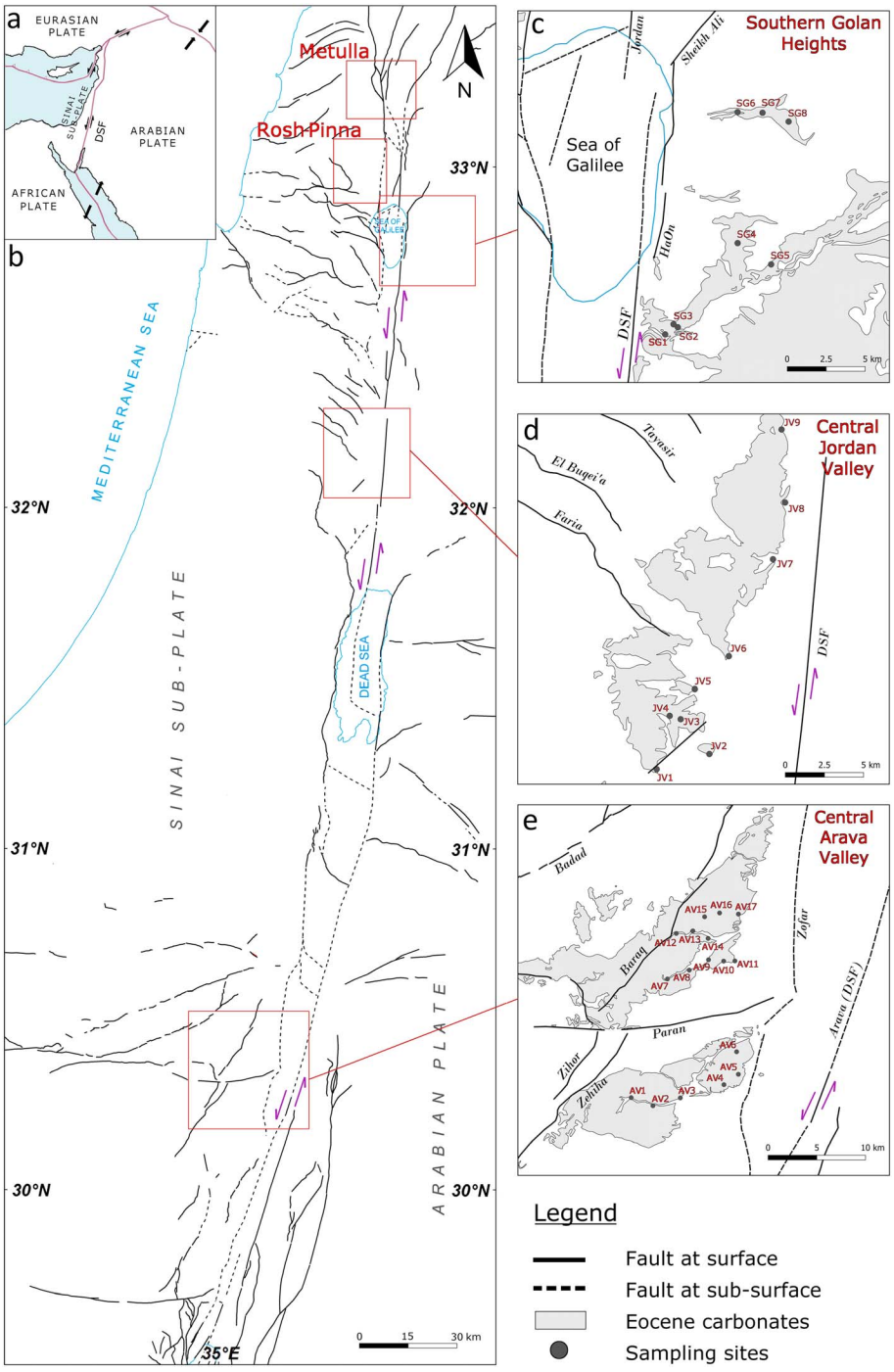

Figure 1. (a) Plate tectonic configuration of the Arabian-African (Sinai) plates. (b) Structures along the southern parts of the DSF (modified from Sneh & Weinberger, 2014) and study areas (red rectangles). (c–e) Generalized geological maps (after Sneh et al., 1998) and sampling sites. DSF = Dead Sea Fault.

1.2. Magnetic Fabrics of Rocks as Strain Indicators

Magnetic fabrics of rocks are commonly used as a strain indicator (e.g., Borradaile, 1991; Borradaile & Henry, 1997; Braun et al., 2015; Cifelli et al., 2013; Levi et al., 2014; Parés et al., 1999; Soto et al., 2007). The Anisotropy of Magnetic Susceptibility (AMS) analysis defines the magnetic fabric. It describes the magnetic susceptibility second-rank tensor with eigenvectors K_1, K_2, and K_3 (maximum, intermediate, and

minimum), which correspond to k_1, k_2, and k_3 eigenvalues. The AMS averages contribution from all crystals and grains in a rock sample and reflects their orientation (Borradaile, 1988). The crystallographic and long axes of grains commonly align coaxially with the principal axes of finite strain, and thus the magnetic fabrics bear structural significance (Borradaile & Jackson, 2010). Correlating the magnetic fabrics with crystal and grain orientations requires knowledge of the rock mineralogy and chemistry.

The texture of calcite-bearing rocks is a sensitive and reliable strain indicator. The *c axes* are usually aligned parallel to the direction of maximum shortening, and this in turn, parallel to the AMS K_3 direction (Bestmann et al., 2000; de Wall et al., 2000; Evans et al., 2003; Owens & Rutter, 1978; Rutter & Rusbridge, 1977). During compaction and lithification processes, some of the *c axes* align with the lithostatic pressure, depending on the pressure magnitude (Hrouda, 2004). Hence, K_3 axes are normal to bedding (vertical), and K_1 and K_2 axes are within the plane of bedding (depositional fabric; e.g., Borradaile & Jackson, 2010). Under tectonic shortening or extension regimes, the AMS axes are generally parallel to the principal strain directions (tectonic fabric; e.g., Borradaile & Jackson, 2010) with K_3 parallel to the direction of maximum shortening and the magnetic fabric is termed "normal" (K_3 parallel to *c-axes*).

Magnetic fabrics of Eocene limestone units along the DSF used as a sensitive strain indicator as they reflect preferred crystallographic orientations of calcite (Issachar et al., 2015; Levi & Weinberger, 2011). In these limestone units, the calcite is diamagnetic as Fe content within the calcite lattices is significantly lower than the threshold of 400 ppm (see Table 2 in Levi & Weinberger, 2011, and Table 1 in Issachar et al., 2015), which may produce "inverse" AMS fabric and paramagnetic behavior (Schmidt et al., 2006). On the other hand, Eocene chalk units along the DSF consist of two main mineralogical components—coccolithic calcite and fibrous clay minerals. Fe content within the calcite lattices is significantly lower than the threshold of 400 ppm (supporting information Table S1). The magnetic fabrics of the chalk are dominated by diamagnetic subfabric of the calcite and paramagnetic subfabric of the clays. By combining AMS measurements at different temperatures, it is possible to separate these subfabrics (Issachar et al., 2018). It was demonstrated that the diamagnetic subfabrics of the chalk reflect preferred crystallographic orientation of calcite and are of tectonic origin, whereas the paramagnetic subfabrics reflect the preferred orientation of clays and tend to preserve the depositional fabric (Issachar et al., 2018).

We analyze the magnetic fabrics of Eocene carbonates in order to reconstruct the strain field in three localities along the southern segment of the DSF. By separating the diamagnetic fabrics in pre-DSF chalk rocks, we systematically infer strain directions along ~400 km of this plate boundary.

2. Geological Setting

2.1. The DSF System

The DSF is an active transform plate boundary between Arabian plate and Sinai subplate (or Africa plate) extending from the Red Sea rift to the convergence zone in southern Turkey (Figure 1a). The left-lateral motion along the DSF takes up most of the opening along the Red Sea and is combined with minor, alternating transtension and transpression (Garfunkel, 2014). Based on mesostructure analysis in Sinai subplate, Eyal and Reches (1983) inferred a DSF-associated stress field with NNW–SSE maximum horizontal shortening (SH_{max}). This stress field is also inferred by Letouzey and Trémolière (1980), Ron and Eyal (1985), Letouzey (1986), and Eyal (1996).

The DSF is a ~1,000-km-long system which can be divided into two main segments: the southern segment extends from the Red Sea rift up to southern Lebanon, and the northern segment from southern Lebanon up to the convergence zone in Turkey (Ben-Avraham, 2014). While the northern segment could hardly be treated as a transform boundary between two rigid plates (Garfunkel, 1981; Nur & Ben-avraham, 1978), the southern segment is marked by a narrow and elongated valley (Picard, 1987; Shimon & Zilberman, 1997) that is associated with several prominent pull-apart basins and left-stepping of the DSF major strands (Garfunkel, 1981). A host of stratigraphic, structural, and geochronological evidence indicates ~107 km of left-lateral offset across the southern segment of the DSF (Bandel, 1981; Bandel & Khoury, 1981; Freund, 1965; Freund et al., 1970; Garfunkel, 1981; Quennell, 1958; Segev, 1984; Sneh & Weinberger, 2003) since the early Miocene (Nuriel et al., 2017). GPS studies of the present plate motions (Sadeh et al., 2012) infer slip rate of 4.6–5.9 mm/year along the southern DSF, compatible with the long-

term slip rates indicated by geological markers (Garfunkel, 2009). About one third of the total offset is associated with a late phase of motion (<5 Ma), which involves a change in the direction of motion of up to ~10° along the southern DSF (Joffe & Garfunkel, 1987). During the late phase, crustal separation along the DSF allowed new surface area produced by normal faulting along the plate margins and the growth of pull-apart basins (Garfunkel, 1981).

Local transtension and transpression led to the development of internal depressions and saddles along the DSF (Garfunkel, 1981; Quennell, 1958). Along the southern segment of the DSF (from south to north), the 180 km long Gulf of Elat (or Aqaba) is the largest and southern-most depression; the 160 km long Arava Valley is characterized by a topographic depression; the 150 km long Dead Sea basin is the deepest depression; the narrow 70 km long central Jordan Valley has a thin sedimentary fill (ten Brink et al., 1999) and records transpression along its southern segment (Gardosh et al., 1990); the 90 km long central and northern Jordan Valley segment comprises the Sea of Galilee-Kinnarot basin, Korazim saddle, and the Hula basin (Garfunkel et al., 1981); and the Metulla Saddle is highly deformed and indicates transpression (Weinberger, 2014; Weinberger et al., 2009).

2.2. Lithology of Eocene Strata

In this paper, we focus on the Eocene Avedat Group, which predates the DSF, in three regions along the southern segment of the DSF: (1) Southern Golan (Figure 1c), (2) Central Jordan Valley (Figure 1d), and (3) Central Arava Valley (Figure 1e). Previous studies focused on Eocene rocks at Metulla (Levi & Weinberger, 2011) and Rosh-Pinna (Issachar et al., 2015) regions (Figure 1b). The Eocene sequence is mainly composed of chalky, occasionally marly, and limestone facies. The chalks are porous, with ~95% (weight) of well-preserved coccolithic calcite and ~5% of clays, quartz, and opal. The limestones are composed of solely coarse calcite grains.

2.3. Southern Golan

The Golan (Figure 1c) is an elevated Miocene-Quaternary basaltic plateau, rising above the western Kinnarot Basin and the Sea of Galilee (Figure 1c). The sedimentary section below the basalt slopes gradually from nearly flat NNW dips in the southern Golan to moderately SSE dips in the northern Golan. In the southern Golan the sedimentary section is slightly deformed (Meiler, 2011) and mainly exposed along the deeply incised streams. To the west, the region is bounded by the N–S strands of the DSF, (e.g., HaOn Fault, Figure 1c).

2.4. Central Jordan Valley

The central Jordan Valley is part of the DSF between Kinnarot Basin to the north and the Dead Sea Basin to the south (Figure 1). The topographic depression in this region narrows up to ~4 km and the young sediment fill is relatively thin (ten Brink et al., 1999). Field observations across the Jericho Fault, ~15 km south to the study area, consist with strike slip and extensional deformation (Hamiel et al., 2018). Ten to 15 km west to the DSF, the Faria Anticline, which is part of the Syrian Arc fold belt (Mimran, 1969), exposes Jurassic and Cretaceous rocks. Several major NW-trending faults (e.g., Faria Fault, Figure 1d) cross the NE-trending anticline and form a series of horsts and grabens (Mimran, 1969). Geophysical studies suggest that these faults are the eastern edge of the Carmel-Gilboa-Faria Fault system, extending to the Mediterranean Sea near the northwestern tip of Mt. Carmel (Ben-Avraham & Ginzburg, 1990; Hofstetter et al., 1996; Segev & Rybakov, 2011). GPS studies suggest that this system absorbs about 15% of the lateral motion along the DSF (Sadeh et al., 2012). Eocene beds on the western shoulders of the valley dip slightly (<10°) eastward. In the northern parts of this section, mid-Eocene limestone dominates, whereas in the southern parts, early Eocene chalk commonly crops out. In the southern parts of the region, Paleogene and Cretaceous sediments are extensively deformed.

2.5. Central Arava Valley

The central Arava Valley is characterized by a topographic depression (Figure 1e). The Arava Fault, in the eastern parts of the region, is considered as the main strand of the DSF, indicating a large left-lateral offset (Frieslander, 2000). Seismic data indicates a ~9-km-wide graben between Arava and Zofar faults that is filled by a few kilometers of Miocene continental beds (Frieslander, 2000). The study area is bounded by the NE-SW trending Zihor-Zehiha-Baraq faults (Avni et al., 2001; Levi, 2003), whose Pleistocene activity was dated

Table 1
Data and Parameters of RT-AMS, LT-AMS and Separated Diamagnetic Fabrics

			RT-AMS						
Area	Site	Rock type	*N*	k_m 10^{-6} SI	Δk 10^{-6} SI	*T*	*Pj*	*L*	*F*
Southern Golan	SG1	Chalk	14	−2.12 (0.45)	0.068 (0.018)	−0.51 (0.476)	1.032 (0.011)	1.024 (0.011)	1.008 (0.010)
	SG2	Chalk	16	7.74 (1.87)	0.161 (0.013)	−0.04 (0.17)	1.021 (0.005)	1.011 (0.004)	1.010 (0.002)
	SG3	Chalk	13	1.93 (1.10)	0.091 (0.022)	−0.17 (0.34)	1.048 (0.031)	1.028 (0.019)	1.020 (0.017)
	SG4	Chalk	12	12.11 (1.54)	0.097 (0.025)	0.39 (0.24)	1.008 (0.002)	1.002 (0.001)	1.006 (0.002)
	SG5	Chalk	20	8.75 (1.90)	0.070 (0.016)	0.75 (0.38)	1.008 (0.003)	1.001 (0.003)	1.007 (0.003)
	SG6	Chalk	10	5.97 (0.63)	0.096 (0.026)	0.20 (0.36)	1.016 (0.006)	1.006 (0.004)	1.010 (0.005)
	SG7	Chalk	15	8.77 (1.40)	0.085 (0.018)	0.25 (0.21)	1.010 (0.003)	1.004 (0.002)	1.006 (0.001)
	SG8	Chalk	5	5.05 (0.79)	0.058 (0.008)	0.22 (0.23)	1.012 (0.001)	1.004 (0.002)	1.007 (0.001)
Central Jordan Valley	JV1	Chalk	7	−4.53 (1.26)	0.065 (0.039)	−0.43 (0.24)	1.014 (0.009)	1.010 (0.006)	1.004 (0.004)
	JV2	Chalk	14	2.19 (2.38)	0.136 (0.049)	−0.05 (0.38)	1.064 (0.109)	1.033 (0.051)	1.030 (0.071)
	JV3	Limestone	20	−7.99 (4.52)	0.139 (0.106)	−0.56 (0.39)	1.018 (0.045)	1.014 (0.033)	1.004 (0.013)
	JV4	Chalk	10	18.71 (5.16)	0.167 (0.067)	0.37 (0.32)	1.009 (0.003)	1.003 (0.002)	1.006 (0.003)
	JV5	Chalk	17	1.76 (2.29)	0.115 (0.025)	−0.24 (0.35)	1.067 (0.199)	1.041 (0.093)	1.026 (0.077)
	JV6	Limestone	19	−11.13 (0.88)	0.082 (0.096)	−0.74 (0.33)	1.007 (0.009)	1.006 (0.002)	1.001 (0.007)
	JV7	Limestone	20	−9.85 (1.12)	0.073 (0.021)	0.00 (0.40)	1.007 (0.003)	1.004 (0.002)	1.004 (0.003)
	JV8	Limestone	9	−11.8 (0.64)	0.044 (0.039)	−0.07 (0.22)	1.004 (0.003)	1.002 (0.002)	1.002 (0.001)
	JV9	Limestone	15	−10.54 (0.75)	0.161 (0.093)	−0.84 (0.26)	1.015 (0.009)	1.014 (0.008)	1.001 (0.003)
Central Arava Valley	AV1	Chalk	15	10.75 (2.00)	0.089 (0.013)	0.02 (0.27)	1.008 (0.002)	1.004 (0.002)	1.004 (0.001)
	AV 2	Chalk	12	−1.26 (0.76)	0.096 (0.006)	−0.07 (0.41)	1.079 (0.162)	1.041 (0.138)	1.037 (0.048)
	AV 3	Chalk	9	−2.80 (1.90)	0.039 (0.010)	0.03 (0.28)	1.014 (0.004)	1.007 (0.004)	1.007 (0.002)
	AV 4	Chalk	14	8.66 (2.14)	0.107 (0.020)	0.41 (0.19)	1.012 (0.003)	1.004 (0.002)	1.009 (0.002)
	AV 5	Chalk	12	4.63 (1.77)	0.070 (0.019)	0.11 (0.40)	1.015 (0.006)	1.007 (0.004)	1.008 (0.006)
	AV 6	Chalk	12	0.47 (1.86)	0.036 (0.029)	−0.36 (0.49)	1.079 (0.097)	1.053 (0.074)	1.025 (0.046)
	AV 7	Chalk	13	−3.91 (0.52)	0.053 (0.015)	−0.44 (0.27)	1.014 (0.005)	1.010 (0.003)	1.004 (0.003)
	AV 8	Chalk	13	−2.01 (0.54)	0.073 (0.019)	−0.31 (0.44)	1.037 (0.012)	1.024 (0.009)	1.013 (0.010)
	AV 9	Chalk	15	−1.11 (0.88)	0.141 (0.013)	−0.27 (0.40)	1.134 (0.635)	1.081 (0.119)	1.049 (0.475)
	AV 10	Chalk	14	2.54 (1.64)	0.114 (0.013)	0.19 (0.29)	1.046 (0.057)	1.018 (0.025)	1.027 (0.032)
	AV 11	Chalk	14	0.10 (2.32)	0.001 (0.020)	−0.49 (0.31)	1.015 (0.011)	1.011 (0.008)	1.004 (0.007)
	AV 12	Chalk	15	−2.51 (0.83)	0.051 (0.015)	−0.20 (0.27)	1.021 (0.010)	1.012 (0.007)	1.008 (0.005)
	AV 13	Chalk	14	−0.50 (3.00)	0.003 (0.018)	−0.13 (0.41)	1.007 (0.009)	1.004 (0.003)	1.003 (0.007)
	AV 14	Chalk	13	0.42 (0.87)	0.015 (0.008)	−0.08 (0.36)	1.037 (0.030)	1.020 (0.023)	1.017 (0.019)
	AV 15	Chalk	14	−4.53 (0.78)	0.031 (0.008)	−0.36 (0.42)	1.007 (0.002)	1.005 (0.002)	1.002 (0.002)
	AV 16	Chalk	14	−1.44 (1.51)	0.087 (0.023)	−0.31 (0.31)	1.062 (0.128)	1.040 (0.070)	1.022 (0.055)
	AV 17	Chalk	12	−1.40 (1.04)	0.067 (0.030)	−0.19 (0.32)	1.049 (0.025)	1.029 (0.021)	1.020 (0.011)

Note. The parameters are calculated from sites mean tensors. *N* is number of samples, k_m is mean susceptibility, Δk is susceptibility difference, *T* is shape of anisotropy, *Pj* is corrected anisotropy degree, *L* is magnetic lineation, *F* is magnetic foliation. RT-AMS = room temperature anisotropy of magnetic susceptibility; LT-AMS = low temperature anisotropy of magnetic susceptibility.

to 400 Ka (Nuriel et al., 2011). The ~W–E trending Paran Fault, which crosses the region, was active from early Miocene (Bartov, 1974; Sakal, 1967) to early Pleistocene (Calvo, 2000). Along the Paran Fault, an elevated ~7 km wide zone shows extensive deformation. Mesozoic units dip steeply, forming an anticline parallel to the fault segment. The Paran Fault shows right-lateral motion (<500 m) combined with vertical displacement (Bartov, 1974; Calvo, 2000; Frieslander et al., 2000). Eocene chalk beds exposed between Zofar and Zihor-Zehiha-Baraq segments dip slightly (<10°) southeastward (Figure 1e).

3. Methods

We analyzed the magnetic fabrics of 461 carbonate samples from 34 sites within three regions along the DSF (Table 1). The room temperature AMS (RT-AMS) was measured at a magnetic field of 450 A/m (average field), which was found more accurate according to measurement errors, and a frequency of 976 Hz with a MFK1-A Kappabridge (AGICO Inc.) at the Institute of Earth Sciences at the Hebrew University of Jerusalem. The low temperature AMS (LT-AMS) was measured according to the procedure presented by Issachar et al. (2016) with a KLY-4S Kappabridge (AGICO Inc.) at the Geological Survey of Israel. The samples were cooled in a liquid nitrogen bath for 50 min before the first measurement, and for 5 min between axial and mean susceptibility measurements. The Kappabridge coil was protected from the cold sample

Table 1 *(continued)*

		LT-AMS					
Area	*N*	k_m 10^{-6} SI	Δk 10^{-6} SI	*T*	*Pj*	*L*	*F*
Southern Golan	5	24.32 (1.63)	0.343 (0.022)	0.725 (0.15)	1.014 (0.001)	1.002 (0.001)	1.012 (0.002)
	4	57.23 (6.93)	0.343 (0.038)	0.73 (0.07)	1.006 (0.000)	1.001 (0.000)	1.005 (0.000)
	5	42.52 (5.18)	0.144 (0.013)	0.63 (0.21)	1.003 (0.000)	1.001 (0.000)	1.003 (0.000)
	5	76.57 (8.84)	0.637 (0.206)	0.73 (0.07)	1.008 (0.002)	1.001 (0.000)	1.007 (0.002)
	3	72.66 (5.84)	0.236 (0.018)	0.72 (0.15)	1.003 (0.000)	1.000 (0.000)	1.003 (0.000)
	5	51.98 (3.55)	0.514 (0.033)	0.69 (0.06)	1.010 (0.001)	1.002 (0.000)	1.008 (0.001)
	5	58.83 (9.46)	0.309 (0.056)	0.44 (0.21)	1.005 (0.001)	1.001 (0.001)	1.004 (0.001)
	3	47.41 (2.75)	0.230 (0.046)	0.73 (0.12)	1.005 (0.001)	1.001 (0.000)	1.004 (0.001)
Central Jordan Valley	5	18.30 (4.73)	0.181 (0.022)	0.69 (0.20)	1.010 (0.010)	1.002 (0.004)	1.008 (0.007)
	5	35.82 (8.75)	0.327 (0.022)	0.68 (0.13)	1.009 (0.003)	1.001 (0.001)	1.008 (0.002)
		-	-	-	-	-	-
	5	107.8 (19.69)	0.494 (0.070)	0.66 (0.03)	1.005 (0.000)	1.001 (0.000)	1.004 (0.000)
	5	41.43 (10.35)	0.417 (0.065)	0.91 (0.14)	1.010 (0.003)	1.000 (0.001)	1.010 (0.002)
		-	-	-	-	-	-
		-	-	-	-	-	-
		-	-	-	-	-	-
		-	-	-	-	-	-
Central Arava Valley	5	62.03 (6.46)	0.285 (0.050)	0.73 (0.21)	1.005 (0.001)	1.001 (0.001)	1.004 (0.000)
	5	21.52 (2.52)	0.076 (0.022)	0.19 (0.40)	1.004 (0.001)	1.001 (0.002)	1.002 (0.001)
	5	20.51 (8.88)	0.239 (0.071)	−0.06 (0.38)	1.012 (0.012)	1.006 (0.008)	1.006 (0.004)
	5	51.34 (7.00)	0.239 (0.033)	0.65 (0.20)	1.005 (0.001)	1.001 (0.001)	1.004 (0.001)
	5	51.11 (8.29)	0.256 (0.025)	0.32 (0.21)	1.005 (0.001)	1.002 (0.000)	1.003 (0.001)
	5	27.80 (5.33)	0.029 (0.002)	0.41 (0.23)	1.007 (0.002)	1.002 (0.000)	1.005 (0.002)
	4	19.75 (1.43)	0.177 (0.006)	−0.43 (0.26)	1.009 (0.002)	1.006 (0.001)	1.003 (0.001)
	5	20.71 (1.99)	0.151 (0.018)	0.57 (0.45)	1.007 (0.002)	1.002 (0.001)	1.006 (0.003)
	5	31.92 (5.17)	0.177 (0.034)	0.20 (0.36)	1.006 (0.002)	1.002 (0.002)	1.003 (0.001)
	5	54.88 (6.96)	0.154 (0.022)	0.12 (0.32)	1.003 (0.001)	1.001 (0.001)	1.002 (0.001)
	5	38.59 (7.57)	0.228 (0.052)	0.60 (0.28)	1.006 (0.002)	1.001 (0.001)	1.005 (0.002)
	5	23.71 (3.21)	0.151 (0.023)	−0.28 (0.39)	1.006 (0.002)	1.004 (0.002)	1.002 (0.001)
	5	42.31 (8.84)	0.106 (0.017)	−0.29 (0.21)	1.002 (0.001)	1.002 (0.001)	1.001 (0.000)
	5	34.01 (2.70)	0.144 (0.019)	0.02 (0.20)	1.004 (0.001)	1.002 (0.001)	1.002 (0.000)
	5	14.48 (3.05)	0.772 (0.014)	−0.56 (0.21)	1.054 (0.076)	1.042 (0.056)	1.012 (0.018)
	4	29.55 (2.68)	0.131 (0.021)	−0.14 (0.24)	1.004 (0.001)	1.003 (0.001)	1.002 (0.001)
	5	27.99 (4.06)	0.046 (0.016)	0.39 (0.55)	1.002 (0.001)	1.001 (0.001)	1.001 (0.001)

with a thin silicon sheet, and the samples were wrapped with a Teflon layer to prevent ice condensation. Mean susceptibility values (k_m) were corrected for liquid nitrogen absorption following Issachar et al. (2016). The RT-AMS shows a composite fabric of diamagnetic and paramagnetic subfabrics. However, when measured at ~77°K, the LT-AMS reflects the paramagnetic subfabric. The diamagnetic subfabric is analytically separable by subtracting the paramagnetic subfabric from the RT-AMS (Issachar et al., 2018).

The AMS principal axes and their 95% confidence ellipses were calculated by a bootstrapping method (1,000 replicates), using the software package Orient 3.6.3 (Vollmer, 2015). We considered only samples that passed the *F* test for 95% confidence interval (>3.9; Jelinek, 1977), or samples in which the principal AMS axes are within the 95% confidence intervals of the site mean tensor. Mean susceptibility ($k_m = k_1 + k_2 + k_3/3$), susceptibility difference ($\Delta k = k_1\text{-}k_3$), corrected degree of anisotropy ($Pj = \exp\sqrt{2\sum(\ln k_i - \ln k_m)^2}$; i = 1 to 3), shape of the AMS ($T = 2\ln(k_2/k_3)/\ln(k_1/k_3) - 1$), magnetic foliation ($F = k_2/k_3$), and magnetic lineation ($L = k_1/k_2$) were calculated according to Jelinek (1981).

4. Results

4.1. General

We measured and analyzed a total of 29 chalk sites (378 samples) and 5 limestone sites (83 samples), in addition to 22 sites (418 samples) of previous studies (Issachar et al., 2015; Levi & Weinberger, 2011). Table 1 shows the AMS parameters of RT-AMS, LT-AMS, and the separated diamagnetic fabrics with

Table 1 *(continued)*

		Separated diamagnetic					
Area	*N*	k_m 10^{-6} SI	Δk 10^{-6} SI	*T*	*Pj*	*L*	*F*
Southern Golan	14	−12.87	0.100 (0.016)	0.56 (0.26)	1.008 (0.001)	1.002 (0.001)	1.006 (0.001)
	16	−12.87	0.106 (0.023)	−0.38 (0.28)	1.008 (0.002)	1.006 (0.002)	1.003 (0.001)
	13	−12.87	0.067 (0.017)	−0.18 (0.41)	1.005 (0.001)	1.003 (0.001)	1.002 (0.002)
	12	−12.87	0.144 (0.014)	0.17 (0.24)	1.011 (0.001)	1.005 (0.001)	1.007 (0.002)
	20	−12.87	0.010 (0.015)	0.05 (0.42)	1.001 (0.001)	1.000 (0.001)	1.000 (0.001)
	10	−12.87	0.129 (0.030)	0.23 (0.38)	1.010 (0.002)	1.004 (0.002)	1.006 (0.002)
	15	−12.87	0.060 (0.015)	−0.45 (0.42)	1.005 (0.001)	1.003 (0.002)	1.001 (0.001)
	5	−12.87	0.056 (0.005)	0.11 (0.33)	1.004 (0.000)	1.002 (0.001)	1.002 (0.001)
Central Jordan Valley	7	−12.87	0.079 (0.042)	0.58 (0.35)	1.006 (0.003)	1.001 (0.002)	1.005 (0.002)
	14	−12.87	0.082 (0.045)	0.06 (0.34)	1.006 (0.004)	1.003 (0.003)	1.003 (0.002)
		-	-	-	-	-	-
	10	−12.87	0.071 (0.046)	0.21 (0.33)	1.006 (0.004)	1.002 (0.002)	1.003 (0.003)
	17	−12.87	0.105 (0.027)	0.10 (0.43)	1.008 (0.002)	1.004 (0.002)	1.005 (0.002)
		-	-	-	-	-	-
		-	-	-	-	-	-
		-	-	-	-	-	-
		-	-	-	-	-	-
Central Arava Valley	15	−12.87	0.058 (0.010)	−0.45 (0.28)	1.005 (0.001)	1.003 (0.001)	1.001 (0.001)
	12	−12.87	0.048 (0.012)	−0.41 (0.27)	1.004 (0.001)	1.003 (0.001)	1.001 (0.001)
	9	−12.87	0.119 (0.018)	−0.51 (0.15)	1.009 (0.001)	1.007 (0.001)	1.002 (0.001)
	14	−12.87	0.025 (0.017)	0.67 (0.22)	1.002 (0.001)	1.000 (0.001)	1.002 (0.001)
	12	−12.87	0.048 (0.027)	−0.09 (0.39)	1.004 (0.002)	1.002 (0.002)	1.002 (0.001)
	12	−12.87	0.047 (0.025)	−0.22 (0.41)	1.004 (0.002)	1.002 (0.002)	1.001 (0.001)
	13	−12.87	0.076 (0.011)	−0.49 (0.32)	1.006 (0.001)	1.004 (0.001)	1.002 (0.001)
	13	−12.87	0.052 (0.015)	−0.27 (0.34)	1.004 (0.001)	1.003 (0.001)	1.001 (0.001)
	15	−12.87	0.052 (0.020)	−0.81 (0.28)	1.004 (0.002)	1.004 (0.001)	1.000 (0.001)
	14	−12.87	0.039 (0.013)	−0.32 (0.56)	1.003 (0.001)	1.002 (0.001)	1.001 (0.001)
	14	−12.87	0.036 (0.020)	0.05 (0.30)	1.003 (0.002)	1.001 (0.001)	1.001 (0.001)
	15	−12.87	0.079 (0.012)	−0.06 (0.29)	1.006 (0.001)	1.003 (0.001)	1.003 (0.001)
	14	−12.87	0.039 (0.016)	−0.01 (0.30)	1.003 (0.001)	1.002 (0.001)	1.002 (0.001)
	13	−12.87	0.046 (0.008)	−0.33 (0.32)	1.004 (0.001)	1.002 (0.001)	1.001 (0.001)
	14	−12.87	0.431 (0.046)	−0.66 (0.04)	1.034 (0.004)	1.028 (0.003)	1.006 (0.001)
	14	−12.87	0.078 (0.023)	−0.22 (0.27)	1.006 (0.002)	1.004 (0.001)	1.002 (0.002)
	12	−12.87	0.061 (0.031)	0.14 (0.38)	1.005 (0.002)	1.002 (0.003)	1.003 (0.001)

the sites mean tensors. Table 2 presents the mean tensors principal orientations and their 95% bootstrap confidence cones. Limestone and chalk samples are distinguished by their mean susceptibility values (Figure 2a). The mean susceptibility values of the limestone samples range between −8 and -12×10^{-6} SI, which are close to the value of pure calcite (which is -12.87×10^{-6} SI; Nye, 1985; Schmidt et al., 2006). The mean susceptibility values of the chalk samples range between −5 and 12×10^{-6} SI. These values indicate that the limestone samples are solely composed of diamagnetic fabric of calcite, whereas the chalk consists additional minerals and may comprise a composite fabric. The susceptibility difference (Δk) of all site mean tensors is about $0.10 \pm 0.02 \times 10^{-6}$ SI (Figure 3). Figure 4 shows the k_m of chalk samples at low temperature ($k_m{}^{LT}$) versus k_m at room temperature ($k_m{}^{RT}$). The positive and high linear correlations of southern Golan and Jordan Valley samples (Figure 4a) and central Arava Valley samples (Figure 4b) indicate that increase in susceptibility is related to increase in paramagnetic contents, whereas diamagnetic and ferromagnetic contents in the samples are almost constant (Issachar et al., 2018). Moreover, the linear regression indicates that the ferromagnetic contribution in the samples is negligible since the point $k_m{}^{LT} = k_m{}^{RT}$ is close to the susceptibility of calcite (Figure 4). Figure 5 shows the inclinations of the AMS K_3 axes of the paramagnetic and diamagnetic subfabrics of the chalk samples. The paramagnetic subfabrics are characterized by bedding-normal K_3 axes, typical of depositional fabrics, whereas the diamagnetic subfabrics are characterized by shallow inclinations of K_3 axes, typical of tectonic fabrics.

Tectonics

10.1029/2018TC005168

Table 2

Mean Tensors Principal Orientations and Their 95% Bootstrap Confidence Cones (Maximum/Minimum) of the RT-AMS, LT-AMS, and the AMS Axes of the Separated Diamagnetic Fabrics, Calculated With 1,000 Replicates

		RT-AMS			LT-AMS			Separated diamagnetic fabrics		
		Principal axes—trend/plunge (95% Conf. angles—max/min)			Principal axes—trend/plunge (95% Conf. angles—max/min)			Principal axes—trend/plunge (95% Conf. angles—max/min)		
Area	Site	K_1	K_2	K_3	K_1	K_2	K_3	K_1	K_2	K_3
Southern Golan	SG1	278/07 (26/6)	007/04 (29/8)	126/82 (7/5)	64/3 (40/4)	333/17 (41/5)	162/73 (4/2)	169/68 (6/5)	303/16 (19/6)	018/19 (37/5)
	SG2	207/03 (11/3)	117/13 (11/7)	312/77 (7/4)	349/09 (14/3)	259/03 (13/3)	146/79 (11/2)	204/21 (15/7)	085/54 (14/6)	306/30 (9/4)
	SG3	272/02 (08/06)	003/32 (11/7)	177/57 (10/7)	357/05 (22/7)	266/15 (20/2)	106/74 (06/3)	088/20 (15/5)	314/63 (14/12)	189/27 (27/9)
	SG4	345/06 (11/6)	076/07 (10/5)	215/81 (6/5)	068/00 (15/1)	388/04 (13/3)	157/86 (3/1)	114/85 (6/3)	340/04 (7/4)	251/07 (14/9)
	SG5	262/02 (126/6)	336/08 (128/8)	161/81 (7/4)	285/03 (−/−)	015/12 (−/−)	181/79 (−/−)	189/49 (109/40)	226/36 (145/63)	049/40 (104/23)
	SG6	286/07 (15/10)	196/08 (15/11)	063/79 (11/11)	247/02 (21/2)	337/06 (21/5)	145/84 (5/2)	224/83 (14/5)	125/01 (14/12)	35/08 (13/5)
	SG7	050/03 (12/4)	141/01 (14/8)	226/85 (8/5)	002/01 (16/5)	272/02 (17/9)	112/88 (10/4)	064/69 (33/8)	247/18 (36/11)	337/01 (11/5)
	SG8	263/16 (21/6)	336/09 (20/8)	109/72 (9/7)	214/16 (−/−)	308/30 (−/−)	118/60 (−/−)	113/43 (10/6)	263/44 (14/8)	007/15 (16/6)
Central Jordan Valley	JV1	147/17 (56/9)	033/10 (124/29)	346/83 (41/9)	254/01 (57/18)	336/17 (49/16)	189/79 (31/14)	197/52 (18/9)	228/26 (40/20)	067/27 (45/11)
	JV2	139/19 (72/8)	020/17 (131/11)	258/77 (15/6)	042/05 (18/6)	113/12 (21/4)	290/76 (7/3)	245/83 (17/10)	323/06 (18/14)	049/05 (20/4)
	JV3	139/16 (68/16)	148/37 (105/27)	032/77 (34/26)	-	-	-	-	-	-
	JV4	132/03 (27/6)	041/16 (27/7)	222/74 (8/5)	060/09 (24/5)	328/09 (22/7)	196/77 (7/5)	136/31 (41/12)	346/35 (57/28)	238/10 (41/9)
	JV5	143/04 (13/3)	051/25 (14/9)	239/65 (8/4)	068/12 (53/7)	158/02 (49/5)	247/77 (5/2)	230/84 (9/4)	320/50 (11/10)	052/05 (11/4)
	JV6	194/22 (26/9)	020/70 (32/8)	291/06 (11/7)	-	-	-	-	-	-
	JV7	093/05 (14/7)	187/42 (18/12)	357/87 (16/11)	-	-	-	-	-	-
	JV8	284/07 (26/12)	029/48 (18/14)	186/43 (27/15)	-	-	-	-	-	-
	JV9	088/39 (132/7)	340/06 (132/11)	245/46 (10/4)	-	-	-	-	-	-
Central Arava Valley	AV1	180/02 (20/4)	090/02 (18/7)	299/88 (5/5)	081/04 (44/2)	356/01 (43/2)	297/86 (6/1)	318/81 (7/41)	175/08 (43/19)	098/12 (38/12)
	AV 2	121/04 (13/4)	283/81 (58/12)	119/85 (57/15)	155/26 (77/30)	301/34 (113/30)	059/81 (64/27)	295/03 (20/6)	027/70 (14/9)	198/30 (19/8)
	AV 3	072/23 (9/6)	178/35 (30/10)	319/46 (24/6)	185/09 (45/7)	090/16 (44/10)	307/69 (13/3)	057/75 (14/2)	265/13 (14/3)	173/07 (3/2)
	AV 4	168/00 (30/4)	258/00 (31/4)	242/89 (4/3)	360/05 (32/6)	270/05 (31/8)	133/84 (7/6)	145/40 (30/14)	304/50 (117/28)	318/55 (43/23)
	AV 5	264/04 (29/5)	174/01 (30/7)	082/85 (6/4)	077/06 (15/3)	168/05 (15/6)	289/82 (7/3)	296/60 (21/7)	182/13 (27/9)	083/18 (15/7)
	AV 6	119/03 (16/4)	210/08 (16/5)	015/82 (5/4)	081/08 (20/9)	174/12 (22/15)	322/77 (19/7)	319/07 (18/12)	218/45 (29/18)	070/61 (33/15)
	AV 7	233/05 (15/6)	143/01 (15/7)	030/86 (7/5)	308/21 (10/4)	215/03 (128/8)	171/67 (59/8)	220/04 (13/4)	124/57 (13/5)	311/33 (5/4)
	AV 8	112/01 (20/5)	022/07 (24/6)	211/83 (6/4)	167/14 (57/8)	257/01 (57/26)	338/76 (18/14)	301/41 (17/9)	067/35 (18/12)	181/29 (12/7)
	AV 9	124/01 (111/5)	031/01 (122/9)	309/85 (7/5)	257/21 (36/8)	162/06 (39/23)	059/65 (19/11)	115/28 (131/6)	020/37 (138/12)	251/44 (11/6)
	AV 10	332/02 (23/3)	242/05 (22/10)	101/86 (9/5)	103/14 (28/5)	010/12 (29/23)	241/72 (23/4)	341/12 (29/8)	235/48 (35/12)	079/44 (11/9)
	AV 11	189/02 (65/7)	099/10 (52/10)	272/83 (8/6)	291/02 (31/7)	020/03 (36/12)	225/85 (13/8)	190/48 (25/8)	360/47 (81/17)	274/07 (35/14)
	AV 12	024/04 (23/7)	113/07 (21/8)	239/83 (9/6)	120/29 (13/10)	360/44 (22/6)	228/35 (17/8)	214/07 (11/3)	311/44 (12/6)	119/45 (8/2)
	AV 13	293/04 (26/9)	203/04 (28/8)	058/84 (9/7)	047/14 (22/7)	306/32 (38/17)	149/56 (27/4)	130/05 (14/7)	221/41 (19/14)	031/48 (14/3)
	AV 14	033/07 (21/5)	125/14 (24/9)	276/76 (9/3)	125/24 (13/8)	031/10 (11/7)	279/64 (13/10)	036/01 (18/5)	305/56 (16/8)	126/36 (8/6)
	AV 15	239/03 (12/9)	150/18 (12/6)	333/73 (11/6)	316/13 (14/5)	217/20 (50/11)	080/67 (54/10)	081/75 (3/1)	215/11 (2/1)	307/11 (1/1)
	AV 16	101/00 (14/5)	012/23 (15/9)	185/69 (11/5)	208/21 (12/3)	304/16 (16/12)	069/63 (16/4)	100/14 (9/5)	353/50 (8/7)	201/38 (7/5)
	AV 17	180/08 (24/8)	272/25 (24/19)	070/65 (14/10)	184/25 (157/21)	279/39 (112/61)	029/59 (84/23)	180/04 (21/9)	269/43 (33/24)	084/52 (27/14)

Note. AMS = Anisotropy of Magnetic Susceptibility; RT-AMS = room temperature AMS; LT-AMS = low temperature AMS.

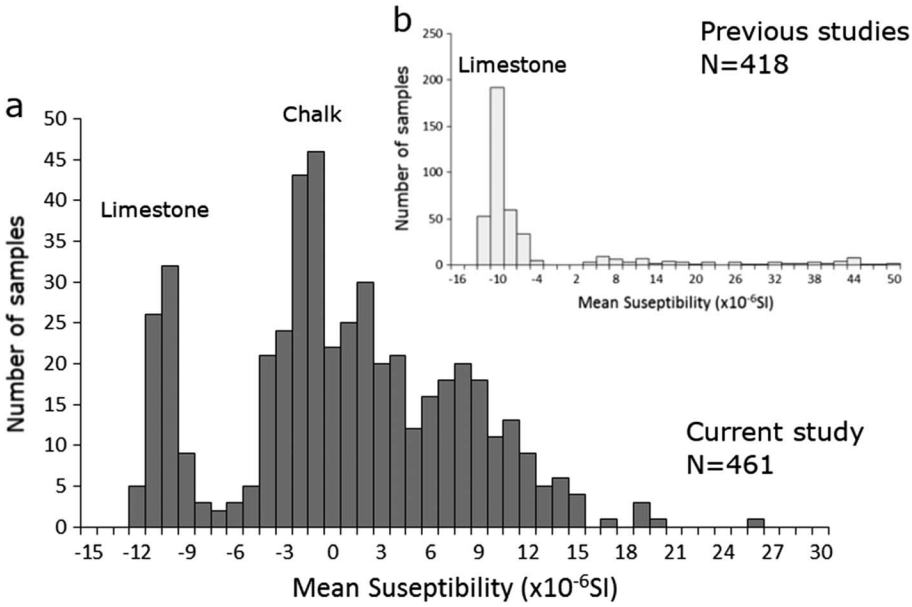

Figure 2. Frequencies of mean susceptibility (k_m) of Eocene samples within the Dead Sea Fault. (a) Current study and (b) previous studies (Issachar et al., 2015; Levi & Weinberger, 2011).

4.2. Southern Golan

The susceptibility values of eight Eocene chalk sites in the southern Golan range between −2 and 12×10^{-6} SI (Table 1). Figure 6a shows the projections of bootstrapping AMS principal axes of the diamagnetic subfabrics. The fabrics are generally characterized by clusters of all AMS axes and subhorizontal K_3 axes, indicating tectonic fabrics, excluding SG5 site in which the dispersion of K_3 axes is too large to allow the type of fabric to be conclusively determined, (i.e., inconclusive fabric). The diamagnetic subfabrics suggest one main group based on the orientation of the horizontal components of K_3 axes (Figure 6b). This group includes five sites (SG1, 3, 6, 7, 8) and indicates an average NNE–SSW (014°/04°) direction of K_3 axes (gray arrows on the map in Figure 6a). Notably, the most distant site from the DSF segments (SG5 site) indicates an inconclusive fabric.

4.3. Central Jordan Valley

The susceptibility values of the five limestone sites (Table 1; JV3, JV6–JV9) in central Jordan Valley range between −11.8 and -8×10^{-6} SI and that of four chalk sites (Table 1; JV1–2, JV4–5) between −4.5 and 18×10^{-6} SI. Figure 7a shows the projections of bootstrapping AMS principal axes of the diamagnetic fabrics

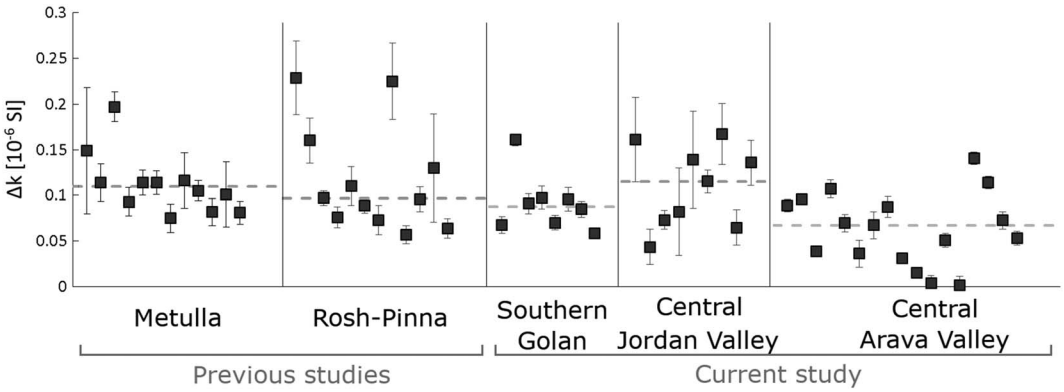

Figure 3. Susceptibility difference (Δk) of site mean tensors of the current and previous studies (Issachar et al., 2015; Levi & Weinberger, 2011). Gray dashed lines indicate median values of the different regions. Error bars indicate site standard deviations.

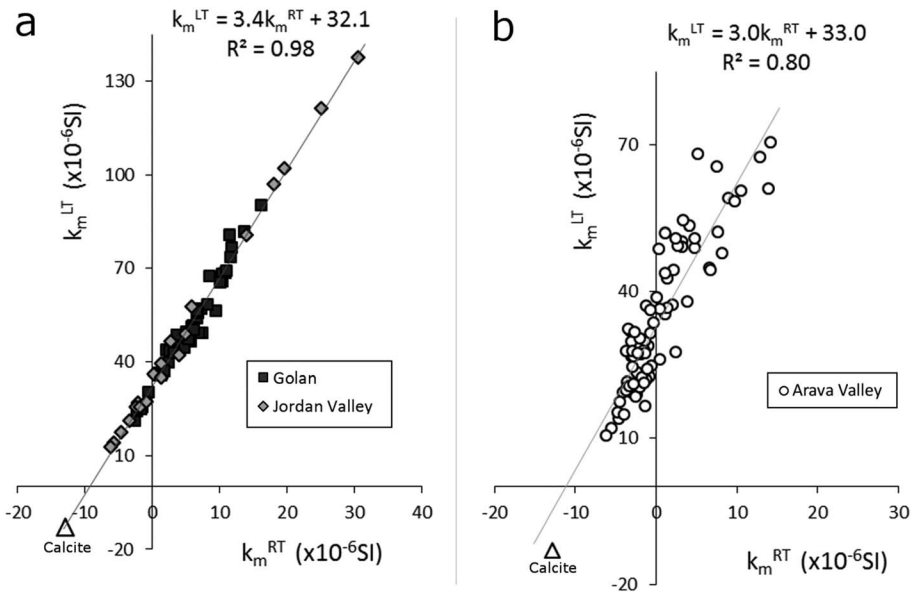

Figure 4. Low temperature mean susceptibility (k_m^{LT}) versus room temperature mean susceptibility (k_m^{RT}) of chalk samples, showing linear correlations. Triangles mark the value of a single calcite crystal. (a) Samples of southern Golan and central Jordan Valley. (b) Samples of central Arava Valley.

of the limestone and subfabrics of the chalk. These generally characterized by clusters of all AMS axes, and subhorizontal K_3 axes, indicating tectonic fabrics. The diamagnetic fabrics and subfabrics suggest one main group based on the orientation of the horizontal components of K_3 axes (Figure 7b). This group includes the diamagnetic subfabrics of five sites (JV1, 2, 4, 5, 9) and indicates an average NE–SW (235°/02°) direction of K_3 axes (white arrows on the map in Figure 7a).

4.4. Central Arava Valley

The susceptibility values of 17 Eocene chalk sites in central Arava Valley range between −4.5 and 10.7×10^{-6} SI (Table 1). Figure 8a shows the projections of bootstrapping AMS principal axes of the diamagnetic subfabrics, which are generally characterized by clusters of all AMS axes and shallow K_3 axes, indicating tectonic fabrics, excluding the AV4 site that indicates an inconclusive fabric. The diamagnetic subfabrics suggest three groups based on the orientation of the horizontal components of K_3 axes (Figure 8b). (1) An average W–E (080°/30°) direction of K_3 axes (AV1, 5, 6, 9, 10, 11, 17), marked by white arrows in Figure 8a. (2) An average N–S (191°/24°) direction of K_3 axes (AV2, 3, 8, 13, 16), marked by gray arrows. (3) An average NW–SE (125°/13°) direction of K_3 axes (AV7, 12, 14, 15), marked by black arrows.

Figure 9 shows a triangular plot (Vollmer, 1990) for K_1 axes of the paramagnetic subfabrics of sites AV7–17 (north of Paran Fault), in which the colors represent the distance of the sites from the Baraq Fault. The distributions are between "point" (P) and "girdle" (G), where point distribution dominants up to ~4.2 km from the Baraq Fault.

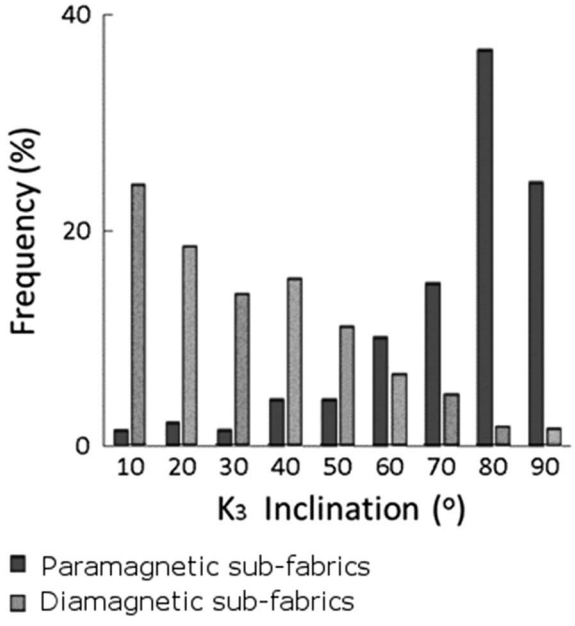

Figure 5. Frequencies of K_3 inclinations of paramagnetic (dark gray) and diamagnetic (light gray) subfabrics of chalk samples.

5. Discussion

5.1. General

In this and previous studies (Issachar et al., 2015; Levi & Weinberger, 2011), the magnetic fabrics of 58 Eocene carbonate sites (i.e., number of cores ~900) in five different regions along the southern segment of the DSF were analyzed. The results are reproducible despite of the low

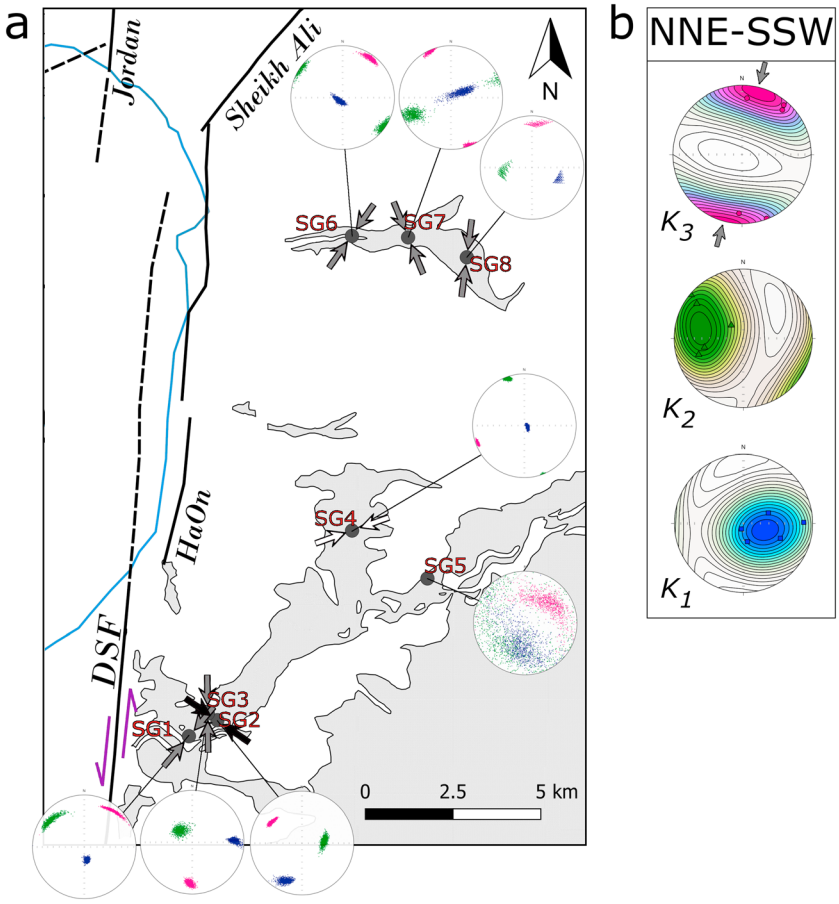

Figure 6. (a) Generalized geological map (after Sneh et al., 1998) and diamagnetic subfabrics of sites in southern Golan. Stereonets of lower-hemisphere, equal-area projection of bootstrapping Anisotropy of Magnetic Susceptibility principal axes (1,000 replicates), K_1 (blue), K_2 (green), and K_3 (pink) axes. Arrows mark the declination of K_3 axes and their colors mark the different orientations. (b) Contours of Anisotropy of Magnetic Susceptibility axes of the main group of sites (SG1, 3, 6, 7, 8) based on the orientations of the horizontal components of K_3 axes. DSF = Dead Sea Fault.

susceptibility values of the carbonate samples. Since calcite-bearing rocks are sensitive and reliable strain indicators, with K_3 axes parallel to maximum shortening (Almqvist et al., 2011; Borradaile et al., 2012; de Wall et al., 2000; Levi & Weinberger, 2011; Owens & Rutter, 1978), the maximum horizontal shortening (SH_{max}) close to the DSF can be estimated. The classification of the magnetic fabrics along the DSF indicates that the vast majority (87%) are of tectonic fabrics, as they characterized by cluster of three susceptibility axes (triaxial) and/or subhorizontal K_3 axes. Only 13% of the magnetic fabrics along the DSF indicate depositional or inconclusive fabrics. Though the magnetic fabrics show clustered K_3 axes at each site, comparison between magnetic fabrics at the study regions shows that the trends of K_3 axes are locally varied. Hence, in order to infer the main trend of strain directions in each region, the K_3 axes of all sites in a region were further statistically analyzed into main groups. In southern Golan and in central Jordan Valley, the distributions of K_3 axes indicate one predominant group (Figures 6b and 7b). On the other hand, in central Arava area three well-distinguished groups of K_3 axes orientations are indicated (Figure 9b).

5.2. Strain Field in Southern Golan

The diamagnetic subfabrics of the southern Golan sites are characterized as tectonic fabrics with main group of K_3 axes orientation in NNE–SSW (Figure 6b). Thus, the magnetic fabrics indicate that SH_{max} in the southern Golan is NNE–SSW, subparallel to the strike of the DSF strands in that region (e.g., HaOn Fault). This strain field may be compatible with subsurface flower structures in the southern Golan (Meiler, 2011; Meiler et al., 2011). Moreover, this strain direction is also obtained in the Rosh-Pinna region, close to the southern

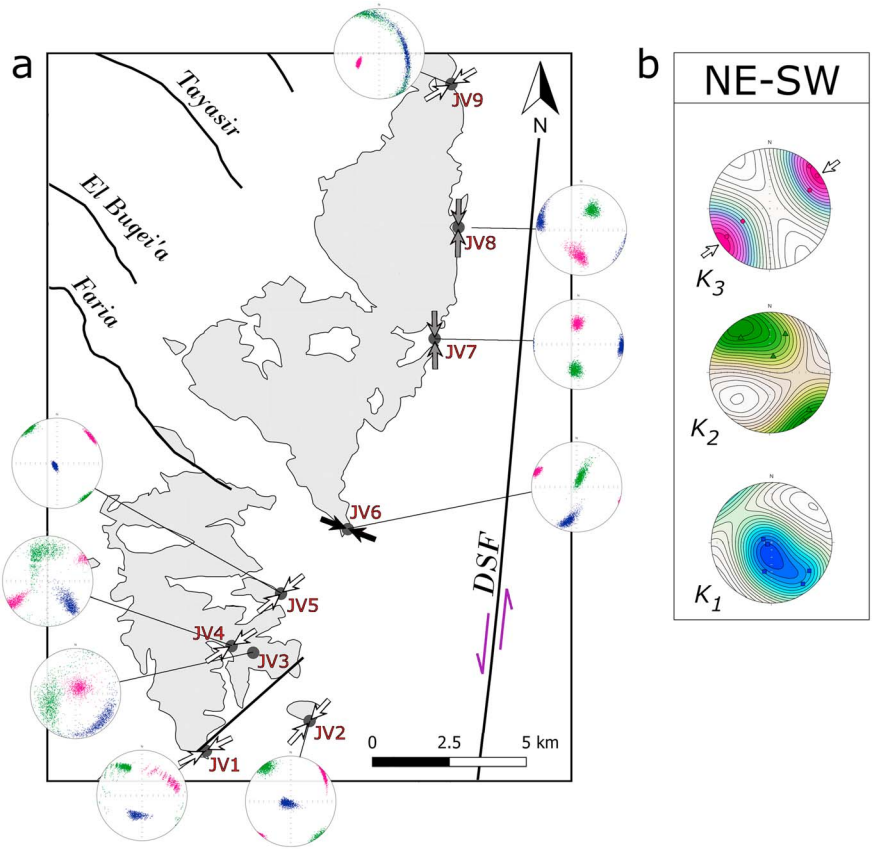

Figure 7. (a) Generalized geological map (after Sneh et al., 1998) and diamagnetic fabrics and subfabrics of study sites in central Jordan Valley. Stereonets of lower-hemisphere, equal-area projection of bootstrapping Anisotropy of Magnetic Susceptibility principal axes (1,000 replicates), K_1 (blue), K_2 (green), and K_3 (pink) axes. Arrows mark the declination of K_3 axes and their colors mark the different orientations. (b) Contours of Anisotropy of Magnetic Susceptibility axes of the main group of sites (JV1, 2, 4, 5, 9) based on the orientations of the horizontal components of K_3 axes. DSF = Dead Sea Fault.

Golan on the Sinai subplate (Figure 1; Issachar et al., 2015). The NNE–SSW SH_{max} direction deviates by ~30° from the NNW–SSE SH_{max} which is associated with the DSF regime since the middle Miocene (Eyal, 1996; Eyal & Reches, 1983). Therefore, we suggest that the NNE-SSW SH_{max} in the southern Golan demonstrates the deflection toward parallelism with strain trajectories toward the major strand of the DSF.

5.3. Strain Field in Central Jordan Valley

The diamagnetic fabrics (limestone) and subfabrics (chalk) of central Jordan Valley sites suggest that the main SH_{max} in this region is ~NE–SW (Figure 7b). This direction was previously suggested by Baer and Mimran (1993) based on paleomagnetic data, which show counterclockwise rotation in Cretaceous rocks of the Faria Anticline. Considering NW–SE to N–S trending faults, which dominate this region, they suggested that counterclockwise rotation might reflect NE–SE shortening regime. Nevertheless, the NE–SW SH_{max} is incompatible with the left-lateral motion along the ~N–S striking DSF (Figure 7a). This direction is perpendicular to the NW–SE faults that dominates the western parts of the region, which considered as the eastern branch of the Carmel-Gilboa-Faria Fault system (Ben-Avraham & Ginzburg, 1990; Hofstetter et al., 1996; Segev & Rybakov, 2011). The ~NE–SW SH_{max} revealed by the magnetic fabrics might result from a local strain field associated with edge effects of the Carmel-Gilboa-Faria Fault system, which can cause a clockwise rotation of the SH_{max} (ten Brink et al., 1996). Notably, the sites, which indicate this direction, are mainly on the southeast tip of the Faria Fault (Figure 7a). The magnetic fabrics of the JV7 and JV8 sites support this proposition, as they are closer to the DSF and indicate N–S trending K_3 axes (Figure 7a).

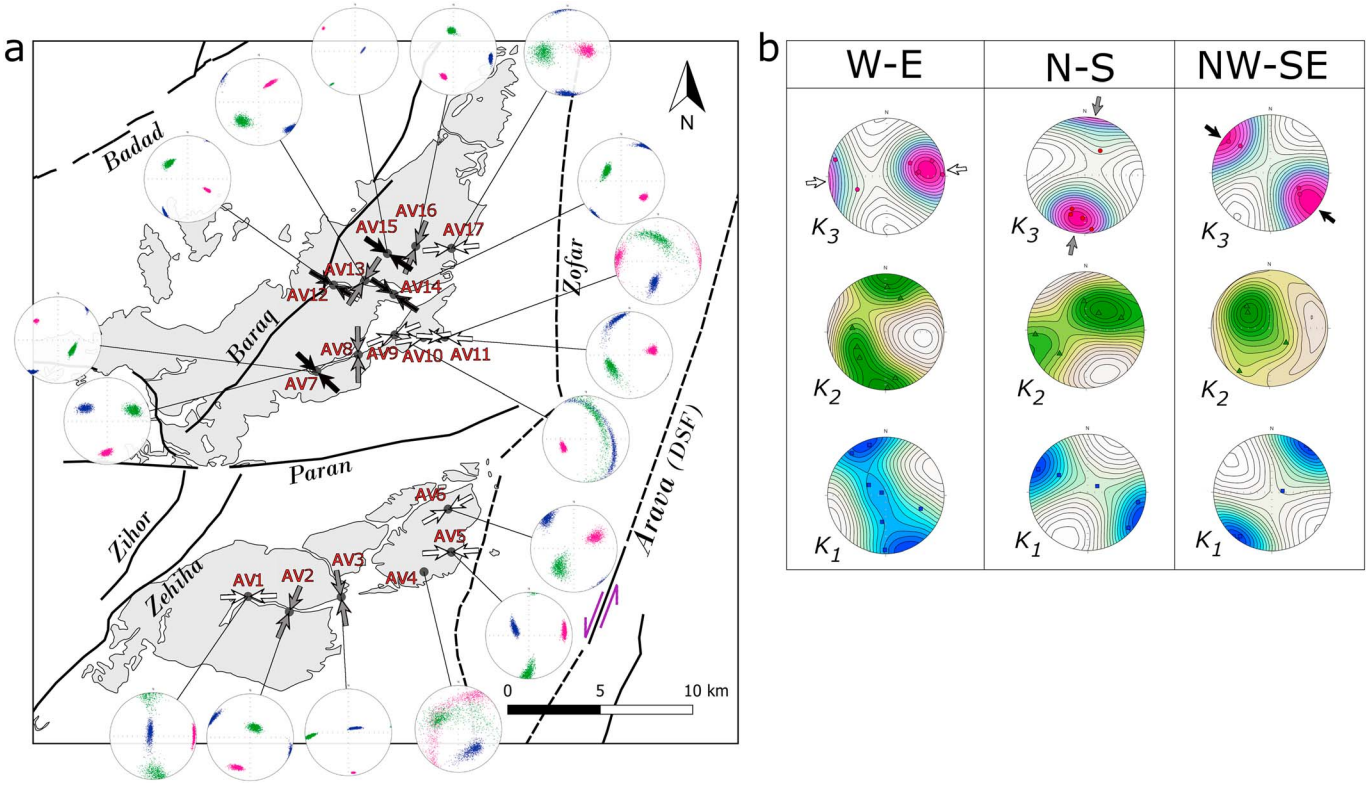

Figure 8. (a) Generalized geological map (after Sneh et al., 1998) and diamagnetic subfabrics of study sites in central Arava Valley. Stereonets of lower-hemisphere, equal-area projection of bootstrapping Anisotropy of Magnetic Susceptibility principal axes (1,000 replicates), K_1 (blue), K_2 (green), and K_3 (pink) axes. Arrows mark the declination of K_3 axes and their colors mark the different orientations. (b) Contours of Anisotropy of Magnetic Susceptibility axes of the main groups of sites based on the orientations of the horizontal components of K_3 axes. DSF = Dead Sea Fault.

5.4. Strain Field in Central Arava Valley

The diamagnetic subfabrics of central Arava Valley sites suggest three predominant SH_{max} directions, based on groups of K_3 axes (Figure 8): (1) W–E, (2) N–S, and (3) NW–SE.

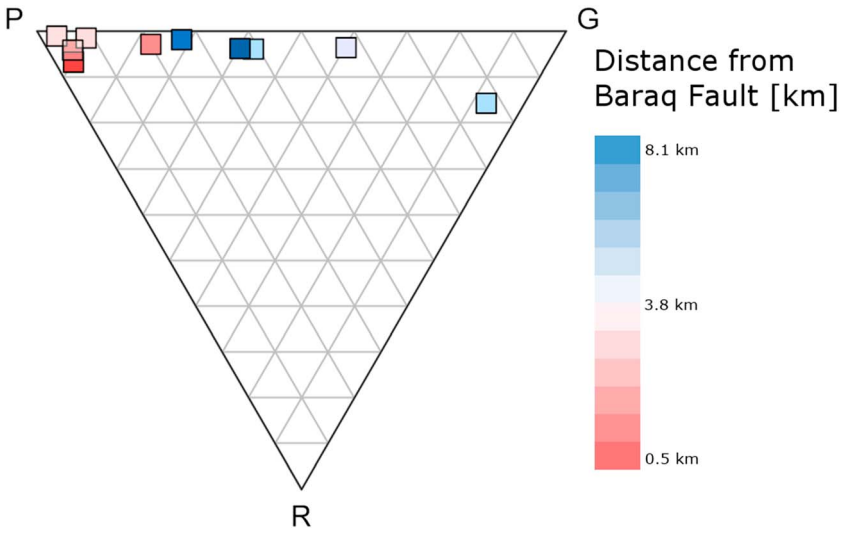

Figure 9. Triangular plot of the paramagnetic subfabrics K_1 axes of central Arava Valley AV7–17 sites. Each square shows the distribution of K_1 axes of a site, between point (P), girdle (G), and random (R) [following Vollmer, 1990]. Colors indicate the distance of the site from the Baraq Fault (Figure 8).

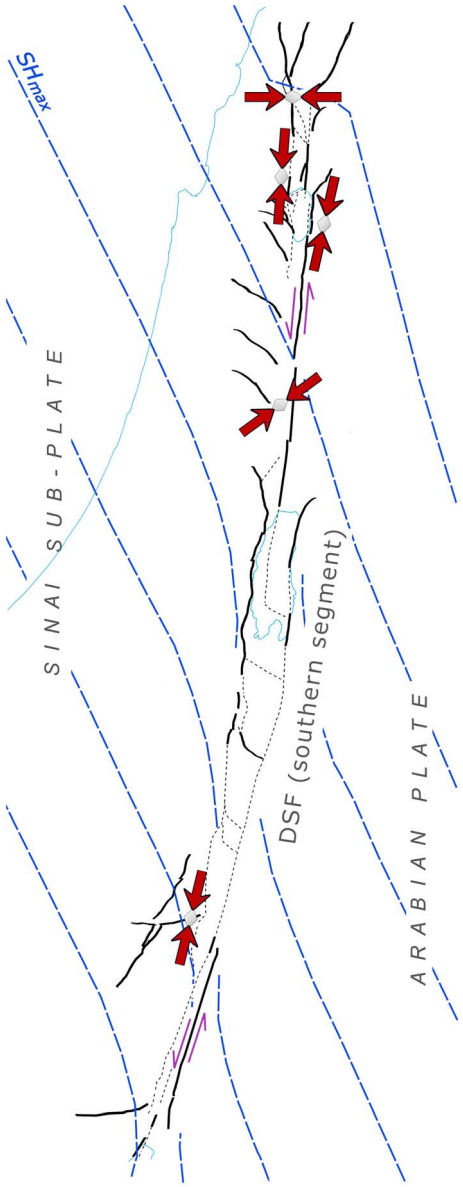

Figure 10. Local and remote SH_{max} directions along the southern segment of the DSF. Red arrows mark the SH_{max} directions interpreted from diamagnetic fabrics. Blue dashed lines represent the SH_{max} and their theoretical deviation close to the DSF (after Garfunkel, 1981). DSF = Dead Sea Fault.

5.4.1. NW–SE SH_{max}

The NW–SE SH_{max} direction (black arrows in Figure 8a) appears mainly near the Baraq Fault. Northwestward thinning of early Eocene groups along the Baraq Fault (Karcz, 1997) and structural reconstruction along the Zihor-Zehiha fault segments (Avni, 1997) suggest reverse motion along these structures in the early-middle Eocene. In addition, based on analysis of NW-striking joint sets in Eocene rocks of central Arava Valley, Levi (2003) suggested that a regional NW–SE SH_{max} was formed during late Eocene. This regional regime was also inferred from joint sets in several Eocene synclines in Israel (Bahat, 1999; Bahat & Grossmann, 1988). The NW–SE SH_{max} direction is perpendicular to the Baraq Fault, and therefore can be associated with its early reverse motion. Moreover, the point distribution of the paramagnetic subfabrics close to the Baraq Fault (Figure 9) supports this conclusion, because the paramagnetic subfabrics do not preserve the depositional fabric, as they do away from faults (Issachar et al., 2018).

5.4.2. W–E SH_{max}

The W–E SH_{max} direction (white arrows in Figure 8a) prevails throughout the region. Three alternative explanations are suggested for this regime: (1) It was associated with the local phase of transpression in the early stage of the DSF activity (Garfunkel, 2014); (2) it was associated with a regional strain field of WNW–ESE SH_{max}, which operated alongside the regional DSF regime (Eyal, 1996); and (3) it was associated with the Miocene motion along the Paran Fault (Sakal, 1967).

Several of observations support the first alternative mentioned above. Tilted basin fill of the Miocene Hazeva Formation, located between Arava and Zofar faults (Calvo, 2002), suggests a phase of local transpression post late Miocene (Garfunkel, 2014). In addition, streams that flowed across the region from east to west, probably during the early Pliocene, suggest a local uplift (Ginat & Avni, 1997), in agreement with pressure ridges near the Arava Fault, a few kilometers north of the study area (Janssen et al., 2011; Kesten, 2004). Subsurface positive flower structures below the ridges (Haberland et al., 2007) also indicate local transpression.

The second alternative of WNW–ESE SH_{max} direction, which is associated with the Syrian Arc fold belt, may have been activated after the Eocene. Originally it was suggested that the Syrian Arc stress field operated from late Cretaceous and terminated during middle Miocene with the initiation of the DSF (Eyal & Reches, 1983; Letouzey & Trémolière, 1980). However, based on trend and age analysis of many structures, Eyal (1996) suggested that Syrian Arc structures were also active after the middle Miocene and up to the recent. He proposed that the two regimes, Syrian Arc and the Dead Sea stress fields, act alternately in spatial and temporal fluctuations.

As for the third alternative, the dextral Paran Fault (Bartov, 1974; Calvo, 2000; Frieslander et al., 2000), which started its lateral motion during early Miocene (Bartov, 1974; Sakal, 1967), ceased its activity in early Pleistocene (Calvo, 2000). The Paran Fault is one of six dextral faults, comprising the Sinai Negev Shear Zone, which is considered to be displaced 107 km by the DSF (Bartov, 1974; Quennell, 1958). According to Eyal and Reches (1983) and Eyal (1996), the dextral slip of the Sinai Negev Shear Zone is compatible with the Syrian Arc regime, namely, WNW–ESE SH_{max}, and thus alternatives (2) and (3) might be considered compatible.

The W–E SH_{max} direction, indicated by the diamagnetic subfabrics in the central Arava Valley, is compatible with the above alternatives, however, the 100°–280° SH_{max} direction of the Syrian Arc regime differs by 20°

from the 080°–260° SH_{max} direction of the diamagnetic subfabrics and therefore this option is excluded. In that manner, the latter direction may represent deflection of strain trajectories in parallel to the Paran Fault. However, this direction is apparent throughout the region and not limited to the proximity of the Paran Fault. Moreover, the sampling sites are at >5 km from the Paran Fault. Considering the dextral slip along the Paran Fault of only a few hundreds of meters (Bartov, 1974), it is unlikely to obtain deflection of the strain field in a few kilometers from the fault segment. We argue that alternative (1) better explains the W–E SH_{max} in the region.

5.4.3. N–S SH_{max}

The N–S SH_{max} direction might be associated with the transtension along the DSF in this region since the Pliocene. Garfunkel (2014) suggests that the present topographic depression of the Arava Valley is an outcome of a change in the tectonic conditions in late Pliocene-Quaternary. The ~N–S striking normal faults (Avni et al., 1994) that accommodate transtension along the DSF in that region support this suggestion. In addition, Levi (2003) based on analysis of a large number of joint sets in Eocene rocks suggested that NNE–SSW SH_{max} and N–S SH_{max} directions are local strain fields associated with the Pleistocene normal motion along the Zihor-Zehiha-Baraq segments and the local extensional strain component near the DSF. This is consistent with U-Th ages of calcite veins (Nuriel et al., 2011) and morphotectonic analysis (Avni et al., 2000), indicating activity of ~400 ka along the Baraq Fault. The N–S SH_{max} direction, indicated by the diamagnetic subfabrics, explains both the increase of transtension along the DSF and the young (<1 Ma) normal activity along the Zihor-Zehiha-Baraq segments.

5.5. Strain Field Along the Southern Segment of the DSF

The SH_{max} directions close to the DSF system, as inferred from the diamagnetic fabrics and subfabrics, suggest that strain directions differ from the remote strain field (Figure 10). Along the southern segment of the DSF, SH_{max} is aligned parallel to the DSF, which expresses local extension (divergence), with the exception of central Jordan Valley in which the strain field may be affected by intersection of two large fault systems. In Metulla region, which is in the transition zone between the southern and the northern segment of the DSF, Levi and Weinberger (2011) found three predominant SH_{max} next to the DSF. They infer Pleistocene to Recent ~E–W SH_{max}, which is compatible with finite strain axes inferred from mesoscale structures, and is expressing local contraction (Weinberger, 2014).

The deviation of the remote strain fields close to the DSF was predicted by Garfunkel (1981) based on extensional structures located along the southern segment of the DSF (blue lines in Figure 10). Seismological observations of focal mechanisms along the southern segment of the DSF show that the dominant left-lateral motion is accompanied by an extensional component, normal to the trace of the DSF (e.g., Salamon et al., 2003). Respectively, Palano et al. (2013) show, based on large and variable seismological data sets, that the seismicity of the southern segment of the DSF is characterized by a combination of strike-slip and normal components. Stress inversions of focal mechanisms suggest that the southern segment of the DSF is characterized by ~NNW–SSE SH_{max} and high stress ratios ($\sigma2–\sigma3/\sigma1–\sigma3$), which is an indicative of strike-slip stress regime that is accompanied also by an extensional component (Hofstetter et al., 2007; Palano et al., 2013). It should be noted that present crustal movements derived from GPS data along the Sinai and Arabian plates (Al-Tarazi et al., 2011; Hamiel et al., 2016; Le Beon et al., 2008; Masson et al., 2015; Palano et al., 2013; Reilinger & Mcclusky, 2011; Sadeh et al., 2012; Wdowinski et al., 2004) does not clearly reflect that the southern segment of the DSF is characterized by a component of normal extension, however this issue was not directly studied yet.

The parallelism of SH_{max} to the DSF inferred by the magnetic fabrics could not be explained by local variations in the geometry of the faults alone, as in these regions no left-stepping of the faults is presented. Moreover, it suggests that deflection of SH_{max} in parallel to the DSF characterizes the entire southern segment of the DSF rather than local transtensive zones. We suggest that the deflection of the strain field close to the DSF is best explained by considering the kinematics of the Sinai-Arabian plates. From that point of view, the theory of rigid plate motion requires migration of the instantaneous pole of rotation over long geological times. An outcome of the pole migration is that the long-term motion along transform boundary cannot be purely strike-slip (Moores & Twiss, 1995, p. 68–69). Garfunkel (1981) and Joffe and Garfunkel (1987) suggested that during the evolution of the DSF, the pole of rotation migrated 4° to 6° east to the pole which best explains the finite motion along the southern segment of the DSF. The instantaneous pole of the past

5 Ma motion calculated by Garfunkel (1981) predicts divergence (transtension) along the southern segment of the DSF and convergence (transpression) along the northern segment of the DSF.

According to the weak fault model (Zoback et al., 1987), the angle of ~20° between the remote (far-field) SH_{max} and the strike of the DSF predicts extension perpendicular to the DSF (Ben-Avraham & Zoback, 1992). Thus, if the southern DSF is a weak boundary, as suggested by Garfunkel (1981) and Ben-Avraham and Zoback (1992), then the prediction of the weak fault model is in good agreement with the kinematic outcome of Sinai-Arabia.

Following these models, we suggest that deflection of SH_{max} parallel to the DSF along its southern segment is a kinematic consequence and is expressing a component of divergence along the southern segment of the DSF.

6. Conclusions

Magnetic fabrics from 58 Eocene carbonate sites in five different regions along the southern parts of the DSF are classified as tectonic fabrics. This indicates that strain localization along transform plate boundaries is manifested in the microstructure of carbonate rocks in its vicinity. The magnetic fabrics suggest that the strain field in the study regions is characterized by one or more dominant orientations. We attributed multiple strain orientations to different stages of deformation (i.e., central Arava and Metulla). The directions of SH_{max} along the southern parts of the DSF since Pliocene time differ from the remote strain field direction that is associated with the DSF regime. Close to the DSF, SH_{max} is subparallel to its trace, indicative of local extension. We interpreted the parallelism of SH_{max} to the DSF trace as a kinematic consequence of divergent motion along the southern segment of the DSF.

Acknowledgments
This study was supported by grants from the Israel Science Foundation 1245/11 and 868/17 to R.W., Israel Science Foundation Center of Excellence grant 1436/14 to S.M., the Israeli Ministry of Energy, and the Naomi Foundation through the Tel Aviv University GRTF Program. We wish to thank the Institute for Rock Magnetism (IRM) for hosting and supporting RI during the course of this study; especially we wish to thank Mike Jackson, Dario Bilardello, and Andrea Biedermann for fruitful discussions and help. The IRM is funded by the NSF Instruments and Facilities program and by the University of Minnesota. We thank Ron Shaar and Yael Ebert for their kind collaboration and help. The assistance in the field of Daniel Zvi, Ran Benyamin, Asaf Ido, Iyad Swaed, Oria Vanunu, and Misha Kitin is highly appreciated. We thank Yehudit Harlavan for her help in analyzing the geochemical data. We thank two anonymous reviewers for providing constructive and very helpful reviews. All the data used for this study are accessible by contacting the authors at ranissachar@gmail.com and available online at https://figshare.com.

References

Almqvist, B. S. G., Hirt, A. M., Herwegh, M., & Leiss, B. (2011). Magnetic anisotropy reveals Neogene tectonic overprint in highly strained carbonate mylonites from the Morcles nappe, Switzerland. *Journal of Structural Geology*, *33*(5), 1010–1022. https://doi.org/10.1016/j.jsg.2011.02.002

Al-Tarazi, E., Abu Rajab, J., Gomez, F., Cochran, W., Jaafar, R., & Ferry, M. (2011). GPS measurements of near-field deformation along the southern Dead Sea Fault System. *Geochemistry, Geophysics, Geosystems*, *12*, Q12021. https://doi.org/10.1029/2011GC003736

Avni, Y. (1997). Geological evolution of the central and southern Negev as an indicator of the evolution of the Dead Sea transform western margin in the late Neogene and Quaternary, (PhD thesis). Hebrew University.

Avni, Y., Bartov, Y., Garfunkel, Z., & Ginat, H. (2000). Evolution of the Paran drainage basin and its relation to the Plio-Pleistocene history of the Arava Rift western margin, Israel. *Israel Journal of Earth Sciences*, *49*(4), 215–238.

Avni, Y., Bartov, Y., Garfunkel, Z., & Ginat, H. (2001). The Arava Formation-A Pliocene sequence in the Arava Valley and its western margin, southern Israel. *Israel Journal of Earth Sciences*, *50*(2–4), 101–120.

Avni, Y., Garfunkel, Z., Bartov, Y., & Ginat, H. (1994). Pleistocene fault system in the central and southern Negev and its implications for the tectonic and geomorphic history of the Arava rift margin. *Israel Journal of Earth Sciences*, *47*(1998), 51–58.

Baer, G., & Mimran, Y. (1993). Paleomagnetism and structural history of the Fari'a anticline, eastern Shomeron. *Current Research-Geological Survey of Israel*, *8*, 58–61.

Bahat, D. (1999). On joints and paleostresses associated with folds along the Syrian Arc in the Negev. *Israel Journal of Earth Sciences*, 29–36.

Bahat, D., & Grossmann, N. F. (1988). Regional jointing and paleostresses in Eocene chalks around Beer Sheva. *Israel Journal of Earth Sciences*, *37*(4), 181–191.

Bandel, K. (1981). New stratigraphic and structural evidence for lateral dislocation in the Jordan rift connected with description of the Jurassic rock column in Jordan. *Neues Jahrbuch für Geologie und Paläontologie*, *161*, 271–308.

Bandel, K., & Khoury, H. (1981). Lithostratigraphy of the Triassic in Jordan. *Facies*, *4*(1), 1–26. https://doi.org/10.1007/BF02536584

Bartov, Y. (1974). A structural and paleogeographical study of the Central Sinai faults and domes, (PhD thesis). Hebrew University.

Ben-Avraham, Z. (1992). Development of asymmetric basins along continental transform faults. *Tectonophysics*, *215*(1–2), 209–220. https://doi.org/10.1016/0040-1951(92)90082-H

Ben-Avraham, Z. (2014). Geophysical studies of the crustal structure along the southern Dead Sea Fault. In *Dead Sea transform fault system: Reviews*, (pp. 1–27). Dordrecht: Springer.

Ben-Avraham, Z., & Ginzburg, A. (1990). Displaced terranes and crustal evolution of the Levant and the eastern Mediterranean. *Tectonics*, *9*(4), 613–622. https://doi.org/10.1029/TC009i004p00613

Ben-Avraham, Z., & Zoback, M. D. (1992). Transform-normal extension and asymmetrie basins: An alternative to pull-apart models. *Geology*, *20*, 423–426. https://doi.org/10.1130/0091-7613(1992)020<0423

Bestmann, M., Kunze, K., & Matthews, A. (2000). Evolution of a calcite marble shear zone complex on Thassos Island, Greece: Microstructural and textural fabrics and their kinematic significance. *Journal of Structural Geology*, *22*(11-12), 1789–1807. https://doi.org/10.1016/S0191-8141(00)00112-7

Borradaile, G. J. (1988). Magnetic-susceptibility, petrofabrics and strain. *Tectonophysics*, *156*, 1–2), 1–20. https://doi.org/10.1016/0040-1951(88)90279-x

Borradaile, G. J. (1991). Corralation of strain with anisotropy of magnetic-susceptibility (AMS). *Pure and Applied Geophysics*, *135*(1), 15–29. https://doi.org/10.1007/bf00877006

Borradaile, G. J., Almqvist, B. S. G., & Geneviciene, I. (2012). Anisotropy of magnetic susceptibility (AMS) and diamagnetic fabrics in the Durness Limestone, NW Scotland. *Journal of Structural Geology*, *34*, 54–60. https://doi.org/10.1016/j.jsg.2011.10.008

Borradaile, G. J., & Henry, B. (1997). Tectonic applications of magnetic susceptibility and its anisotropy. *Earth-Science Reviews*, *42*(1–2), 49–93. https://doi.org/10.1016/S0012-8252(96)00044-X

Borradaile, G. J., & Jackson, M. (2010). Structural geology, petrofabrics and magnetic fabrics (AMS, AARM, AIRM). *Journal of Structural Geology*, *32*(10), 1519–1551. https://doi.org/10.1016/j.jsg.2009.09.006

Braun, D., Weinberger, R., Eyal, Y., Feinstein, S., Harlavan, Y., & Levi, T. (2015). Distinctive diamagnetic fabrics in dolostones evolved at fault cores, the Dead Sea transform. *Journal of Structural Geology*, *77*, 11–26. https://doi.org/10.1016/j.jsg.2015.05.007

Calvo, R. (2000). Stratigraphy and petrology of the Hazeva Formation in the Arava and the Negev, (PhD thesis, in Hebrew). Hebrew University.

Calvo, R. (2002). Stratigraphy and petrology of the Hazeva formation in the Arava and the Negev, *Isr. Geol. Surv. Rep*., doi: GSI/22/2002.

Cifelli, F., Mattei, M., Rashid, H., & Ghalamghash, J. (2013). Right-lateral transpressional tectonics along the boundary between Lut and Tabas blocks (Central Iran). *Geophysical Journal International*, *193*(3), 1153–1165. https://doi.org/10.1093/gji/ggt070

de Wall, H., Bestmann, M., & Ullemeyer, K. (2000). Anisotropy of diamagnetic susceptibility in Thassos marble: A comparison between measured and modeled data. *Journal of Structural Geology*, *22*(11–12), 1761–1771. https://doi.org/10.1016/s0191-8141(00)00105-x

Dewey, J. F., Holdsworth, R. E., & Strachan, R. A. (1998). Transpression and transtension zones. *Geological Society of London, Special Publication*, *135*(1), 1–14. https://doi.org/10.1144/GSL.SP.1998.135.01.01

Evans, M. A., Lewchuk, M. T., & Elmore, R. D. (2003). Strain partitioning of deformation mechanisms in limestones: Examining the relationship of strain and anisotropy of magnetic susceptibility (AMS). *Journal of Structural Geology*, *25*(9), 1525–1549. https://doi.org/10.1016/S0191-8141(02)00186-4

Eyal, Y. (1996). Stress field fluctuations along the Dead Sea rift since the middle Miocene. *Tectonics*, *15*(1), 157–170. https://doi.org/10.1029/95TC02619

Eyal, Y., & Reches, Z. (1983). Tectonic analysis of the Dead Sea rift region since the Late-Cretaceous based on mesostructures. *Tectonics*, *2*(2), 39–66.

Fossen, H. (2010). *Structural geology*. New York: Cambridge University Press. https://doi.org/10.1017/CBO9780511777806

Fossen, H., Tikoff, B., & Teyssier, C. (1994). Strain modeling of transpressional and transtensional deformation. *Norsk Geologisk Tidsskrift*, *62*(3), 195–204. https://doi.org/10.1016/S0164-1212(01)00142-X

Freund, R. (1965). Structural consequences of Dead Sea strike-slip fault. *Israel Journal of Earth Sciences*, *13*(3–4), 163.

Freund, R., Garfunkel, Z., Zak, I., Goldberg, M., Weissbrod, T., & Derin, B. (1970). The shear along the Dead Sea rift. *Philosophical Transactions of the Royal Society A*, *267*(1181), 107–130. https://doi.org/10.1098/rsta.1970.0027

Frieslander, U. (2000). The structure of the Dead Sea transform emphasizing the Arava using new geophysical data, (PhD thesis). Hebrew University.

Frieslander, U., Bruner, I., & Bartov, Y. (2000). 3D Mapping of Karkom Graben, *Isr. Geol. Surv. Rep*., doi: GSI/11/2000.

Gardosh, M., Reches, Z., & Garfunkel, Z. (1990). Holocene tectonic deformation along the western margins of the Dead Sea. *Tectonophysics*, *180*(1), 123–137. https://doi.org/10.1016/0040-1951(90)90377-K

Garfunkel, Z. (1981). Internal structure of the Dead Sea leaky transform (rift) in relation to plate kinematics. *Tectonophysics*, *80*(1-4), 81–108. https://doi.org/10.1016/0040-1951(81)90143-8

Garfunkel, Z. (2009). The long- and short-term lateral slip and seismicity along the Dead Sea transform: An interim evaluation. *Israel Journal of Earth Sciences*, *58*(3), 217–235. https://doi.org/10.1560/IJES.58.3-4.217

Garfunkel, Z. (2014). Lateral motion and deformation along the Dead Sea transform. In *Dead Sea transform Fault System: Reviews* (Vol. 6, pp. 109–145). Dordrecht: Springer.

Garfunkel, Z., Zak, I., & Freund, R. (1981). Active faulting in the Dead Sea rift. *Tectonophysics*, *80*, 1–26. https://doi.org/10.1016/0040-1951(81)90139-6

Ginat, H., & Avni, Y. (1997). The Arava conglomerate: A Pliocene valley deposit crossing the Dead Sea rift. *Geological Society of Israel Research*, *9*, 59–62.

Gomez, F., Khawlie, M., Tabet, C., Nasser Darkal, A., Khair, K., & Barazangi, M. (2006). Late Cenozoic uplift along the northern Dead Sea transform in Lebanon and Syria. *Earth and Planetary Science Letters*, *241*(3–4), 913–931. https://doi.org/10.1016/j.epsl.2005.10.029

Haberland, C., Maercklin, N., Kesten, D., Ryberg, T., Janssen, C., Agnon, A., Weber, M., et al. (2007). Shallow architecture of the Wadi Araba fault (Dead Sea transform) from high-resolution seismic investigations. *Tectonophysics*, *432*(1–4), 37–50. https://doi.org/10.1016/j.tecto.2006.12.006

Hamiel, Y., Piatibratova, O., & Mizrahi, Y. (2016). Creep along the northern Jordan Valley section of the Dead Sea fault. *Geophysical Research Letters*, *43*, 2494–2501. https://doi.org/10.1002/2016GL067913

Hamiel, Y., Piatibratova, O., Mizrahi, Y., Nahmias, Y., & Sagy, A. (2018). Crustal deformation across the Jericho Valley section of the Dead Sea fault as resolved by detailed field and geodetic observations. *Geophysical Research Letters*, *45*, 3043–3050. https://doi.org/10.1002/2018GL077547

Hofstetter, A., van Eck, T., & Shapira, A. (1996). Seismic activity along fault branches of the Dead Sea-Jordan transform system: The Carmel-Tirtza fault system. *Tectonophysics*, *267*(1–4), 317–330. https://doi.org/10.1016/S0040-1951(96)00108-4

Hofstetter, R., Klinger, Y., Amrat, A. Q., Rivera, L., & Dorbath, L. (2007). Stress tensor and focal mechanisms along the Dead Sea fault and related structural elements based on seismological data. *Tectonophysics*, *429*(3–4), 165–181. https://doi.org/10.1016/j.tecto.2006.03.010

Hrouda, F. (2004). Problems in interpreting AMS parameters in diamagnetic rocks. *Geological Society of London, Special Publication*, *238*, 49–59.

Issachar, R., Levi, T., Lyakhovsky, V., Marco, S., & Weinberger, R. (2016). Improving the method of low-temperature anisotropy of magnetic susceptibility (LT-AMS) measurements in air. *Geochemistry, Geophysics, Geosystems*, *17*, 2940–2950. https://doi.org/10.1002/2016GC006339

Issachar, R., Levi, T., Marco, S., & Weinberger, R. (2015). Anisotropy of magnetic susceptibility in diamagnetic limestones reveals deflection of the strain field near the Dead Sea fault, northern Israel. *Tectonophysics*, *656*, 175–189. https://doi.org/10.1016/j.tecto.2015.06.021

Issachar, R., Levi, T., Marco, S., & Weinberger, R. (2018). Separation of diamagnetic and paramagnetic fabrics reveals strain directions in carbonate rocks. *Journal of Geophysical Research: Solid Earth*, *123*, 2035–2048. https://doi.org/10.1002/2017JB014823

Janssen, C., Romer, R. L., Hoffmann-Rothe, A., Kesten, D., & AL-Zubi, H. (2011). The Dead Sea transform: Evidence for a strong fault? *Journal of Geology*, *112*(5), 561–575. https://doi.org/10.1086/422666

Jelinek, V. (1977). *The statistical theory of measuring anisotropy of magnetic susceptibility of rocks and its application* (pp. 1–88). Brno: Geofyzika.

Jelinek, V. (1981). Characterization of the magnetic fabric of rocks. *Tectonophysics*, *79*(3–4), T63–T67. https://doi.org/10.1016/0040-1951(81)90110-4

Joffe, S., & Garfunkel, Z. (1987). Plate kinematics of the circum Red Sea—A re-evaluation. *Tectonophysics*, *141*(1–3), 5–22. https://doi.org/10.1016/0040-1951(87)90171-5

Karcz, Z. (1997). The Geology of the North Paran Region, (PhD thesis, in Hebrew). Hebrew University.

Kesten, D. (2004). Structural observations at the Southern Dead Sea transform from seismic reflection data and ASTER satellite images at Potsdam, (PhD thesis). Geoforschungszentrum.

Le Beon, M., Klinger, Y., Amrat, A. Q., Agnon, A., Dorbath, L., Baer, G., et al. (2008). Slip rate and locking depth from GPS profiles across the southern Dead Sea transform. *Journal of Geophysical Research*, *113*, B11403. https://doi.org/10.1029/2007JB005280

Letouzey, J. (1986). Cenozoic paleo-stress pattern in the Alpine Foreland and structural interpretation in a platform basin. *Tectonophysics*, *132*(1-3), 215–231. https://doi.org/10.1016/0040-1951(86)90033-8

Letouzey, J., & Trémolière, P. (1980). Paleo-stress fields around the Mediterranean since the Mesozoic from microtectonics. Comparison with plate tectonic data. In *Tectonic Stresses in the Alpine-Mediterranean Region* (pp. 173–192). Vienna: Springer. https://doi.org/10.1007/978-3-7091-8588-9_18

Levi, T. (2003). Joint set as a tool for analyses the tectonic deformation in the central Arava western rift margin, (Msc thesis, in Hebrew). Ben Gurion University.

Levi, T., & Weinberger, R. (2011). Magnetic fabrics of diamagnetic rocks and the strain field associated with the Dead Sea fault, northern Israel. *Journal of Structural Geology*, *33*(4), 566–578. https://doi.org/10.1016/j.jsg.2011.02.001

Levi, T., Weinberger, R., & Marco, S. (2014). Magnetic fabrics induced by dynamic faulting reveal damage zone sizes in soft rocks, Dead Sea basin. *Geophysical Journal International*, *199*(2), 1214–1229. https://doi.org/10.1093/gji/ggu300

Masson, F., Hamiel, Y., Agnon, A., Klinger, Y., & Deprez, A. (2015). Variable behavior of the Dead Sea fault along the southern Arava segment from GPS measurements. *Comptes Rendus Geoscience*, *347*(4), 161–169. https://doi.org/10.1016/j.crte.2014.11.001

Meiler, M. (2011). The deep geological structure of the Golan Heights, (PhD thesis). Tel-Aviv University.

Meiler, M., Reshef, M., & Shulman, H. (2011). Seismic depth-domain stratigraphic classification of the Golan Heights, central Dead Sea fault. *Tectonophysics*, *510*(3-4), 354–369. https://doi.org/10.1016/j.tecto.2011.08.007

Mimran, Y. (1969). The geology Wadi El-Malih, (PhD thesis). Hebrew University.

Moores, E., & Twiss, R. (1995). *Tectonics*. New York: W. H. Freeman and Company.

Mount, V. S., & Suppe, J. (1987). State of stress near the San Andreas fault: Implications for wrench tectonics. *Geology*, *15*(12), 1143–1146. https://doi.org/10.1130/0091-7613(1987)15<1143

Nur, A., & Ben-avraham, Z. (1978). The eastern Mediterranean of continental collision and the Levant: Tectonics of continental collision. *Tectonophysics*, *46*(3–4), 297–311. https://doi.org/10.1016/0040-1951(78)90209-3

Nuriel, P., Rosenbaum, G., Uysal, T. I., Zhao, J., Golding, S. D., Weinberger, R., Karabacak, V., et al. (2011). Formation of fault-related calcite precipitates and their implications for dating fault activity in the east Anatolian and Dead Sea fault zones. *Geological Society of London, Special Publication*, *359*(1), 229–248. https://doi.org/10.1144/SP359.13

Nuriel, P., Weinberger, R., Kylander-Clark, A. R. C., Hacker, B. R., & Craddock, J. P. (2017). The onset of the Dead Sea transform based on calcite age-strain analyses. *Geology*, *45*(7), 587–590. https://doi.org/10.1130/G38903.1

Nye, J. F. (1985). *Physical properties of crystals: Their representation by tensors and matrices*. New York: Oxford University Press.

Owens, W. H., & Rutter, E. H. (1978). The development of magnetic susceptibility anisotropy through crystallographic preferred orientation in a calcite rock. *Physics of the Earth and Planetary Interiors*, *16*(3), 215–222. https://doi.org/10.1016/0031-9201(78)90014-6

Palano, M., Imprescia, P., & Gresta, S. (2013). Current stress and strain-rate fields across the Dead Sea fault system: Constraints from seismological data and GPS observations. *Earth and Planetary Science Letters*, *369-370*, 305–316. https://doi.org/10.1016/j.epsl.2013.03.043

Parés, J. M., van der Pluijm, B. A., & Dinares-Turell, J. (1999). Evolution of magnetic fabrics during incipient deformation of mudrocks (Pyrenees, northern Spain). *Tectonophysics*, *307*(1-2), 1–14. https://doi.org/10.1016/S0040-1951(99)00115-8

Picard, L. (1987). The Elat (Aqaba)-Dead Sea-Jordan subgraben system. *Tectonophysics*, *141*(1–3), 23–32. https://doi.org/10.1016/0040-1951(87)90172-7

Quennell, A. M. (1958). Tectonics of the Dead Sea rift. In *Proceedings of the 20th International Geological Congress, Mexico* (pp. 386–405). Mexico City.

Reilinger, R., & Mcclusky, S. (2011). Nubia–Arabia–Eurasia plate motions and the dynamics of Mediterranean and Middle East tectonics. *Geophysical Journal International*, *186*, 971–979. https://doi.org/10.1111/j.1365-246X.2011.05133.x

Ron, H., & Eyal, Y. (1985). Intraplate deformation by block rotation and mesostructures along the Dead Sea transform. *Tectonics*, *4*, 85–105.

Rutter, E. H., & Rusbridge, M. (1977). The effect of non-coaxial strain paths on crystallographic preferred orientation development in the experimental deformation of a marble. *Tectonophysics*, *39*(1–3), 73–86. https://doi.org/10.1016/0040-1951(77)90089-0

Sadeh, M., Hamiel, Y., Ziv, A., Bock, Y., Fang, P., & Wdowinski, S. (2012). Crustal deformation along the Dead Sea transform and the Carmel fault inferred from 12 years of GPS measurements. *Journal of Geophysical Research*, *117*, B08410. https://doi.org/10.1029/2012JB009241

Sakal, Y. (1967). Geology of the Rekhes Menucha, (Msc thesis). Hebrew Univercity.

Salamon, A., Hofstetter, A., Garfunkel, Z., & Ron, H. (2003). Seismotectonics of the Sinai subplate—The eastern Mediterranean region. *Geophysical Journal International*, *155*(1), 149–173. https://doi.org/10.1046/j.1365-246X.2003.02017.x

Schmidt, V., Gunther, D., & Hirt, A. M. (2006). Magnetic anisotropy of calcite at room-temperature. *Tectonophysics*, *418*(1–2), 63–73. https://doi.org/10.1016/j.tecto.2005.12.019

Segev, A. (1984). Lithostratigraphy and paleogeography of the marine Cambrian sequence in southern Israel and southwestern Jordan. *Israel Journal of Earth Sciences*, *33*, 26–33.

Segev, A., & Rybakov, M. (2011). History of faulting and magmatism in the Galilee (Israel) and across the Levant continental margin inferred from potential field data. *Journal of Geodynamics*, *51*(4), 264–284. https://doi.org/10.1016/j.jog.2010.10.001

Shimon, W., & Zilberman, E. (1997). Systematic analysis of the large-scale topography and structure across the Dead Sea rift. *Tectonics*, *16*(3), 400–424.

Sneh, A., Bartov, Y., Weissbrod, T., &Rosensaft, M. (1998). Geological map of Israel, Scale 1: 200,000, *Geol. Surv. Isr., Jerusalem*.

Sneh, A., & Weinberger, R. (2003). Geology of the Metulla quadrangle, northern Israel: Implications for the offset along the Dead Sea rift. *Israel Journal of Earth Sciences*, *52*(3–4), 123–138. https://doi.org/10.1560/1G3J-NX0H-KBL3-RUY9

Sneh, A., & Weinberger, R. (2014). Major structures of Israel and Environs, scale 1: 500,000, *Geol. Surv. Isr., Jerusalem*.

Soto, R., Casas-Sainz, A. M., Villalain, J. J., & Oliva-Urcia, B. (2007). Mesozoic extension in the Basque-Cantabrian basin (N Spain): Contributions from AMS and brittle mesostructures. *Tectonophysics*, *445*(3-4), 373–394. https://doi.org/10.1016/j.tecto.2007.09.007

ten Brink, U. S., Katzman, R., & Lin, J. A. (1996). Three-dimensional models of deformation near strike-slip faults. *Journal of Geophysical Research*, *101*(B7), 16,205–16,220. https://doi.org/10.1029/96JB00877

ten Brink, U. S., Rybakov, M., Al-Zoubi, A. S., Hassouneh, M., Frieslander, U., Batayneh, A. T., Goldschmidt, V., et al. (1999). Anatomy of the Dead Sea transform: Does it reflect continuous changes in plate motion? *Geology*, *27*(10), 887–890. https://doi.org/10.1130/0091-7613(1999)027<0887:AOTDST>2.3.CO;2

Tikoff, B., & Teyssier, C. (1994). Strain modelling of displacement field partitioning in transpressional orogens. *Journal of Structural Geology*, *16*(11), 1575–1588. https://doi.org/10.1016/0191-8141(94)90034-5

Vollmer, F. W. (1990). An application of eigenvalue methods to structural domain analysis. *Geological Society of America Bulletin*, *102*(6), 786–791. https://doi.org/10.1130/0016-7606(1990)102<0786:AAOEMT>2.3.CO;2

Vollmer, F. W. (2015). Orient 3: Spherical projection and orientation data analysis program. Retrieved from www.frederickvollmer.com/orient

Wdowinski, S., Bock, Y., Baer, G., Prawirodirdjo, L., Bechor, N., Naaman, S., et al. (2004). GPS measurements of current crustal movements along the Dead Sea fault. *Journal of Geophysical Research*, *109*, B05403. https://doi.org/10.1029/2003JB002640

Weinberger, R. (2014). Pleistocene strain partitioning during transpression along the Dead Sea transform, Metulla saddle, northern Israel. In *Dead Sea transform fault system: Reviews* (pp. 151–182). Dordrecht: Springer.

Weinberger, R., Gross, M., & Sneh, A. (2009). Evolving contractional deformation along a plate boundary transform: Example from the Dead Sea fault in northern Israel. *Tectonics*, *28*, TC5005. https://doi.org/10.1029/2008TC002316

Zoback, M. D., Zoback, M. L., Mount, V. S., Suppe, J., Eaton, J. P., Healy, J. H., et al. (1987). New evidence on the state of stress of the San Andreas fault system. *Science*, *238*(4830), 1105–1111. https://doi.org/10.1126/science.238.4830.1105